Scaling and Transition Effects on Hollow-Cylinder/Flare SBLIs in Wind Tunnel Environments

James Threadgill, Christoph Hader, Ashish Singh, Vasilis Tsakagiannis, Hermann Fasel, Jesse Little, Mathieu Lugrin, Reynald Bur, Giuseppe Chiapparino, Christian Stemmer

Scaling and Transition Effects on Hollow-Cylinder/Flare SBLIs in Wind Tunnel Environments

James Threadgill*, Christoph Hader†, Ashish Singh‡, Vasilis Tsakagiannis§, Hermann F. Fasel¶
Department of Aerospace and Mechanical Engineering, University of Arizona, Tucson, AZ 85721, USA

Jesse C. Little‖
Mechanical and Aerospace Engineering Department, The Ohio State University, Columbus, OH 43210, USA

Mathieu Lugrin**, Reynald Bur††
DAAA, ONERA, Université Paris Saclay, F-92190 Meudon, France

Giuseppe Chiapparino‡‡, Christian Stemmer§§
Lehrstuhl für Aerodynamik und Strömungsmechanik, Technische Universität München, Boltzmannstr. 15, D-85747 Garching b. München, Germany

A comprehensive investigation into the flow over a Hollow-Cylinder/Flare (HCF) has been conducted at Mach 5 with $\mathrm{Re}_L \approx 11 \times 10^5$ and a flare deflection $\theta = 15°$. Experiments of two similar models have been conductedi in LT5 at the University of Arizona (Tucson, USA) and R2Ch at ONERA (Meudon, France). Despite similar non-dimensional scaling of the models, a considerable difference in reattachment behavior was observed from Infrared Thermography (IRT) measurements, indicating that the reattachment in LT5 was located approximately twice as far from the flare base as observed in R2Ch. This discrepancy has driven the investigation in an attempt to identify the cause of this difference. Simulations have been performed at the University of Arizona, ONERA, and the Technical University of Munich (Germany) in support of this study, targeting a range of potential factors that are relevant to the challenge, to quantify the various influences. Amongst the effects reviewed are: differences in the freestream Mach number (M_∞) modulating boundary layer development and the flare-induced inviscid pressure rise, differences in the wall temperature conditions (T_w/T_0) also affecting boundary layer development, 3D relief effects due to different normalized cylinder diameters (D/L), differences in the bluntnesses of the two nominally sharp configurations (r_{nose}/L), and the impact of freestream disturbances. The noise environment appears to play a significant role in scaling the Shock Boundary Layer Interaction (SBLI) by affecting the transition behavior along the separated shear layer and causing the bubble to grow/shrink to accommodate. Simulations show that the amplitude can be modulated to control the SBLI size, and produce a close match to the experimental results. However, the distribution of noise in the frequency spectra remains unclear. Experimental investigation of the respective noise environment between the two facilities showed that despite each tunnel exhibiting similar noise magnitudes (expressed as $p'/\bar{p}_\infty$) they differed considerably in the range of frequencies (by a factor of 6.5 when considering freestream Strouhal number), suggesting additional parameters are required when quantifying wind tunnel freestream noise conditions beyond its simple amplitude. This study was conducted as part of an international collaborative effort in support of NATO STO AVT-346 Research Task Group.

*Assistant Professor, AIAA Senior Member (email: jthreadgill@arizona.edu)
†Assistant Research Professor, AIAA Member
‡Postdoctoral Research Associate, AIAA Member
§Graduate Student, AIAA Student Member
¶Professor, AIAA Fellow
‖Professor, AIAA Associate Fellow
**Research Scientist
††Research Director
‡‡Research Associate
§§TUM Adjunct Professor, DGLR member

I. Introduction

Early efforts aimed to classify SBLI according to location of transition within the interaction. Based on Chapman et al. [1]'s classification, fully laminar or turbulent interactions are defined by the location of transition either completely downstream of re-attachment or upstream of separation respectively. Transitional interactions on the other hand are characterized by having the transition location between separation and re-attachment. While turbulent interactions are common at low Mach numbers, laminar and transitional interactions are of practical interest in the hypersonic flight regime.

The use of an axisymmetric geometry to study laminar/transitional SBLIs is motivated by both flight relevance and practical limitations. Early experimental investigations into the effect of boundary layer transition in the presence of a SBLI was carried out by Becker and Korycinski [2] over an ogive-cylinder-flare geometry at Mach 6.8. Since then numerous experimental studies on geometries such as hollow cylinder flare ([3–10]), cone-cylinder-flare ([11–14]) and cone-flare ([15–18]) have been undertaken. While many of these studies observe qualitatively similar flow features, for example the presence of streaks near re-attachment, discrepancies in quantitative comparisons are hard to pin down due to the many unquantified factors (geometry, wind tunnel noise environment, leading edge/nose bluntness etc.) between these efforts.

The configuration itself pertains to that of a naturally evolving zero-pressure gradient boundary layer subject to a single external surface deflection, resulting in a large separated SBLI. The Mach number is equal to 5 to maintain similar compressibility-associated instability mechanisms. The incoming flow is typically laminar, but transition may occur at some point within the SBLI or aft of reattachment. While many angles of external deflection have been considered, this paper is focused on a $\theta = 15^\circ$ deflection, since this creates a large separated region with interesting discrepancies observed between cases. Reynolds numbers are kept within the range required to induce transitional effects, at $\mathrm{Re}_L < 2 \times 10^7$ (where L is the boundary layer evolution length up to the base of the deflection. In this parameter range, the physics of the flow is very rich, with both global instabilities in the recirculation region [19–21] and multiple convective instabilities. First, in the attached boundary layer region, because of the high boundary layer edge Mach number, close to 5 depending on the model leading edge thickness, which could play an important role in such flows [22], one could expect both first and second Mack mode instabilities, then, after the boundary layer separate due to the SBLI, the mixing layer will support shear-layer instabilities [8], which display similar characteristics to first mode waves [23]. Finally, streaks will appear in the reattachment region, possibly due to multiple mechanisms, either linked to global modes [19], to baroclinic effects [24], to non-linear effects [23] or to Görtler type instabilities [25]. Given the rich physics of the flow, and the multiple different mechanisms at play, one could expect free-stream disturbances to play an important role in selecting and seeding the physics. As such, this configuration offers a very good platform to compare experimental results and assess the impact of the discrepancies between experimental setups. In addition, it is the intent to keep geometries as fundamental/simplified as possible to avoid additional scaling considerations, so configurations will be 'non-dimensionalized', *i.e.* that the incoming boundary layer is the only relevant external scaling length. Within this scope, the HCF geometry is to be considered across experiments and simulations.

The HCF is essentially an axisymmetric analogy to the flat-plate-ramp where the flat-plate surface is offset parallel to an axis of rotation. This allows for an easier integration in the wind tunnel test section and nullify the impact of the sides of the flat plate. However, the axisymmetry induces an additional scaling parameter related to the base curvature, and takes away from its true definition as non-dimensional. The influence of this curvature decreases as the diameter of the cylinder increases relative to its length. As such, provided that the diameter is large enough, the flow can be treated as 'quasi-non-dimensional'. This base curvature acts to weaken conical shocks due to area relief experienced downstream. Spanwise/azimuthal locking of integer wavelengths is still a concern, but the influence can be mitigated if the cylinder perimeter is significantly long when compared to the wavelength in question.

This paper outlines recent collaborative efforts undertaken on similar geometries as part of the NATO STO AVT-346 Research Task Group. The data presented herein are assembled to probe into core flow physics, while identifying potential wind tunnel and simulation framework specific issues.

II. Methodology

A. Experiments

1. University of Arizona

Experimental tests have been conducted in the Mach 5 Ludwieg Tube (LT5) at the University of Arizona (UA). This facility consists of a long driver tube with a length of 25.4 m (83.3 ft) and an internal diameter of 406 mm (16.0 inch), heated to avoid oxygen liquefaction during runs (see Figure 1). The driver tube connects to an axisymmetric convergent-divergent nozzle with a length from throat to nozzle exit of 3.0 m (120 in), before entering the 381 mm (15.0 inch) diameter test section of length 892 mm (35.1 inch). Downstream of the test section are two aluminum diaphragms that separate the pre-run pressurized upstream section of the tunnel from a vacuum tank. The tunnel run is initiated by varying the pressure between the diaphragms until they rupture at the required driver tube conditions. Nominal run conditions are listed in Table 1. Note, stagnation temperatures (T_0) are measured within the driver tube during the test and are notably cooler than the quasi-steady pre-run driver tube temperature.

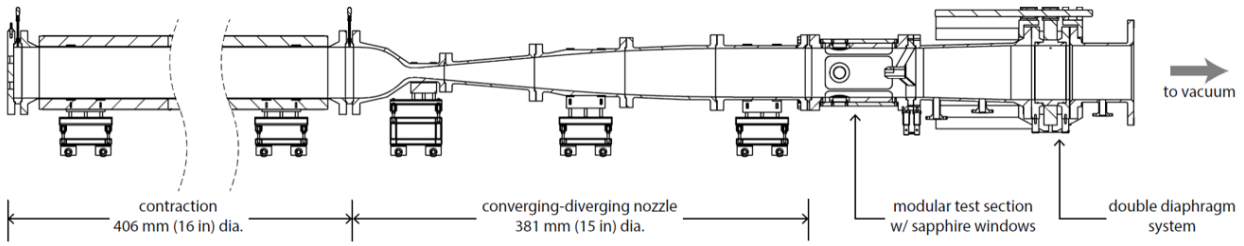

Fig. 1 Schematic diagram of LT5.

M_∞	T_0	U_∞	p_0, kPa (psia)		$\mathrm{Re}'/10^6$, m^{-1} (ft^{-1})		$\mathrm{Re}_L/10^5$
4.82	433 K (320 F)	846 m/s (2777 ft/s)	380	(55)	6.5	(2.0)	12
			510	(74)	8.8	(2.7)	16
			846	(123)	14.5	(4.4)	26
			1211	(176)	20.8	(6.3)	37

Table 1 Constant-operational test conditions in LT5.

The test article geometry has been developed from other 177.8 mm (7.00 inch) diameter hollow cylinder models used in the facility [9], sharing a common 17-4PH stainless steel leading edge ring with radius 102 μm (0.004 inch)[26], internal inverted-cone half-angle deflection of 10°, and internal diameter 149.4 mm (5.88 inch). The outer surface of the steel section is cylindrical and measures 108.0 mm (4.25 inch) in length. The leading edge is located 96.6 mm (3.80 inch) downstream of the nozzle exit plane.

A one-piece 3D-printed cylinder-flare is secured downstream of the leading edge ring. This component was printed from Formlabs' glass-filled 'Rigid 10k' resin and features a 69.9 mm (2.75 inch) extension of the cylinder followed by a 15° flare. Thus, the total cylinder length is 177.8 mm (7.00 inch) with normalized diameter of $D/L = 1$. Due to limitations of the Formlabs 3L print volume the streamwise extent of the flare was made to vary around the circumference. The upper half of the model ($-90° < \phi < +90°$) is axially symmetric with flare outer radius of 106.7 mm (4.20 inch), while the radial limit for the lower half blends into an ellipse with semi-minor axis of 91.4 mm (3.60 inch). The conical face of the flare surface remains axisymmetric, with a half-angle of 15°. See [10] for further details of the configuration.

2. ONERA

The ONERA HCF model is a modernized version of the model used by Benay et al. [4]. The cylinder is $L = 252$ mm long and is followed by a 15° flare, the total length of the cylinder-flare geometry is 350 mm. The external diameter of the cylinder is 138 mm. For practical reasons, starting of the wind tunnel and protection of the instrumentation mainly, the model has an inner diameter of 108 mm and a cylindrical prolongation of 50 mm after the end of the flare. The model is made from Isotan, and is painted with a special black paint to allow the proper measurements of surface temperature

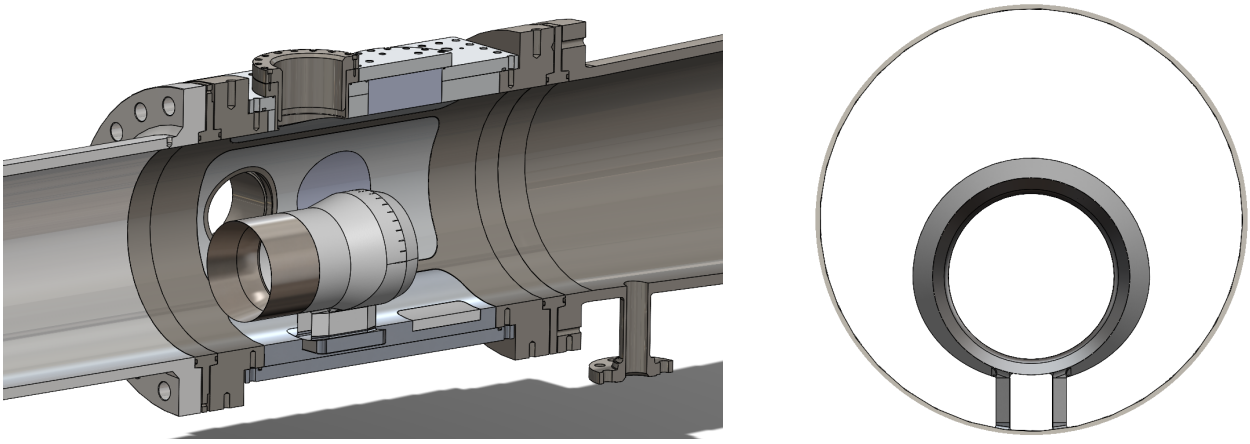

(a) Assembly mounted in sectioned view of LT5.

(b) Axial view of assembly in LT5.

Fig. 2 Images of the cylinder-flare assembly.

via thermal imaging using a FLIR SC7600 InSb camera. The emissivity of the paint has been measured to be 0.85 and the thermal properties of both the paint layer and the Isotan are very well known, allowing for a precise computation of heat-fluxes from the temperature history [27]. After painting, the model has a surface rugosity of $Ra < 3.2\mu m$. The leading edge of the model is considered sharp ($27.5 \pm 1\ \mu$m). The model is equipped with 4 PCB132A31 sensors (located in the reattachment region at $x/L = 1.07, 1.09, 1.10, 1.12$) and 7 Kulite XCQ-093–1PSID sensors (located at $x/L = 0.79, 0.87, 1.07, 1.09, 1.10, 1.12, 1.25$) which are acquired using a NI-PXIe 6376 running at 3.3 MHz and a 6358 running at 1.1MHz respectively. The Kulite signal is filtered analogically and amplified using an ANS E300 signal amplifier/conditioner with a low-pass filter with a cutoff frequency of 100kHz before acquisition. The PCB sensors are mounted using the method described in [8]. The model is also equipped with 52 pressure taps which are distributed along the whole geometry to allow for a precise description of the mean separation bubble, those pressure taps are connected to two ESP32 pressure scanners.

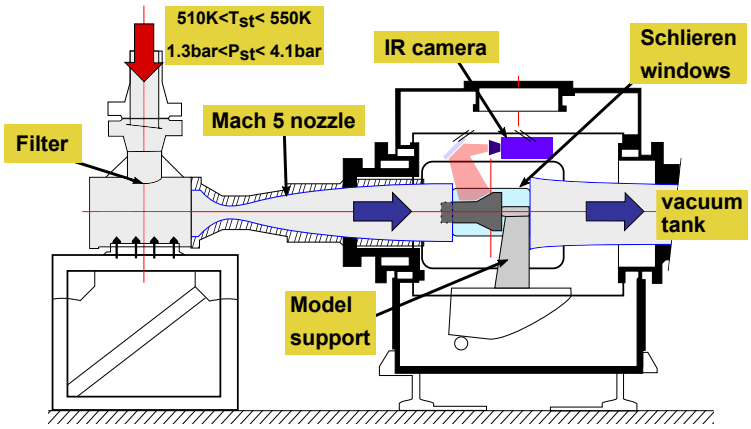

Fig. 3 Schematic of the ONERA HCF model inside R2Ch with the main parameters. Reprinted from Lugrin et al. [8]

The model was tested in the R2Ch facility located on the ONERA Meudon site (see figure 3). It is a conventional blowdown facility that allows to create Mach 5, 6 and 7 flows with contoured nozzles of exit diameter 327 mm. The air generation system can supply air from less than an atmosphere to up to 80 bar and up to 750 K for durations of up to a minute. The facility is connected to a vacuum sphere of 500 m^3 for low Reynolds number runs. In the present case, most of the runs (around 50 runs were conducted) are at a Mach number of 5 for a stagnation pressure of less than 6.5 bar. The different runs from [8] used in this article are presented in table 2

M_∞	Run	T_0, K (F)	U_∞, m/s (ft/s)	p_0, kPa (psi)	$\mathrm{Re}'/10^6$, m^{-1} (ft^{-1})	$\mathrm{Re}_L/10^5$
5	1	504 (448)	919 (3014)	127 (18.4)	1.6 (4.8)	4
	2	503 (446)	918 (3011)	129 (18.7)	1.6 (4.9)	
	1	524 (484)	937 (3073)	241 (35.0)	2.8 (8.6)	7
	2	525 (485)	938 (3076)	225 (32.6)	2.6 (8.0)	
	1	547 (525)	957 (3140)	414 (60.0)	4.5 (13.9)	11
	2	553 (536)	962 (3157)	408 (59.2)	4.4 (13.4)	
		±0.16%	±0.08%	±0.38%	±0.46%	

Table 2 Mean free-stream conditions computed on a 2-second window during the high-frequency acquisition from [8] (maximum normalized standard deviations for each parameter shown beneath the table). The nominal Reynolds numbers (Re_L) are each computed from run 1.

B. Simulations

1. University of Arizona

For the stability and transition calculations for the hollow cylinder flare geometry (Fig. 2), the same simulation strategy (Fig. 4) that has been successfully used for previous numerical investigations of the laminar-turbulent transition process for high-speed boundary layers was employed (see for example Laible et al. [28], Mayer et al. [29], Sivasubramanian and Fasel [30], Hader and Fasel [31]). It can be broken down into three main steps. First, an initial, undisturbed base flow including the leading edge of the geometry is obtained from a precursor calculation (Step 1, Fig. 4). The commercial code CFD++, distributed by Metacomp Technologies (for details see Chakravarthy et al. [32]) was used for Step 1. Once a converged based flow is obtained in Step 1 the base flow is re-converged on a subdomain in Step 2. Convergence in this context means achieving grid convergence (grid independence) as well as converging to a steady state solution. In the second step, a higher-order finite-difference (FD) calculation (for details on the numerical methods see Laible et al. [28]) is performed (Step 2, Fig. 4). For the FD calculation, the computational domain starts downstream of the leading edge of the geometry. For this step, the solution obtained on Step 1 is interpolated onto a finer grid and then used in the FD calculation as initial condition and for the inflow and free-stream boundary condition. This FD calculation is performed in order to obtain a “clean” base flow state for the final third step. In the third step the disturbance (transition) simulations are carried out using the same FD code as in Step 2 (Fig. 4). The re-converged base flow from the second step is used as an initial condition. The disturbances in Step 3 (Fig. 4) can be introduced with different methods. Here, a random forcing approach is used as a model for "natural" transition (Hader and Fasel [33]).

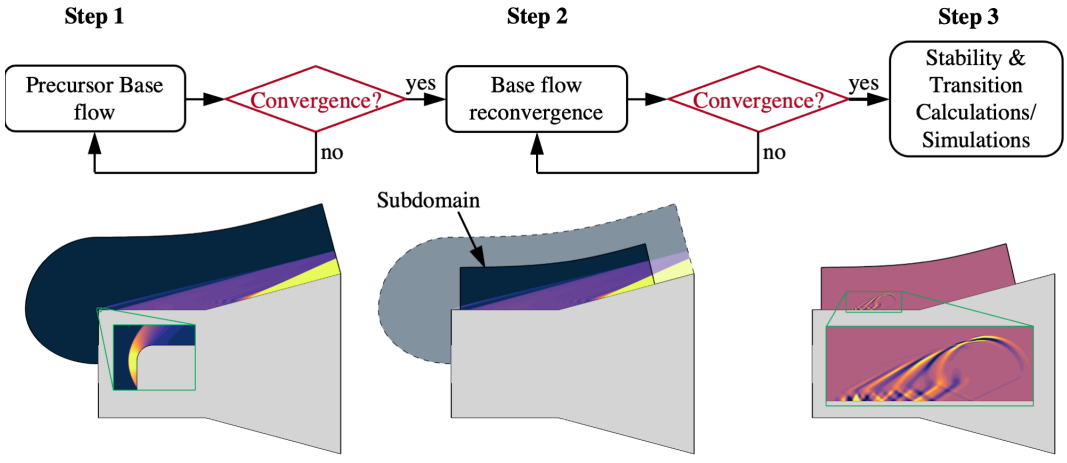

Fig. 4 Simulation strategy for stability and transition simulations.

2. ONERA

Multiple high-fidelity simulations were conducted at ONERA on the ONERA HCF geometry. The chosen configuration is a reproduction of the $Re_L = 1.1 \times 10^6$ run from Lugrin et al. [8] (run 1). The free-stream Mach number is $M_\infty = 5$ and the stagnation temperature and pressure are the one from the wind tunnel run : $T_{st} = 547$ K, $P_{st} = 4.14 \times 10^5$ Pa respectively. All the simulations were conducted using the FastS solver from ONERA, which is a HPC oriented, finite volume multiblock solver working on structured mesh. A structured mesh of $1600 \times 220 \times 1800$ points spanning over an angular section of 180° of the cylinder-flare configuration with periodic boundary conditions is used. This large domain ensures that the selection of the dominant instabilities is not impacted by the selective filtering of the azimuthal wavenumber imposed by the periodicity. To simplify the computation, the leading edge is supposed to be perfectly sharp and is thus not meshed. Standard supersonic inflow, farfield and outflow conditions are used and the temperature of the no-slip wall is fixed to 290 K to better reproduce the experimental setup. The grid spacings correspond to the DNS best practice, even in the turbulent region (Δ_r^+ at wall< 0.5, $\Delta_x^+ < 8$, $r\Delta_\theta^+ < 5$). Convective fluxes are solved using a second-order low dissipation scheme based on the work of Mary and Sagaut [34] and an unlimited third order MUSCL reconstruction. Viscous fluxes are computed using a second order centered scheme. The time integration is conducted explicitly using a three step third order low memory Runge Kutta method. Different Mach and Reynolds number were studied numerically, using different meshes, spanning over various azimuthal angles. In order to trigger convective instabilities (see for instance the work of Hader and Fasel [33]), all simulations were perturbed by injecting a white noise on density at the inlet of the domain. Different amplitude were considered to study the impact of the free-stream noise on the flow. The random disturbance approach used here is similar to the one presented by

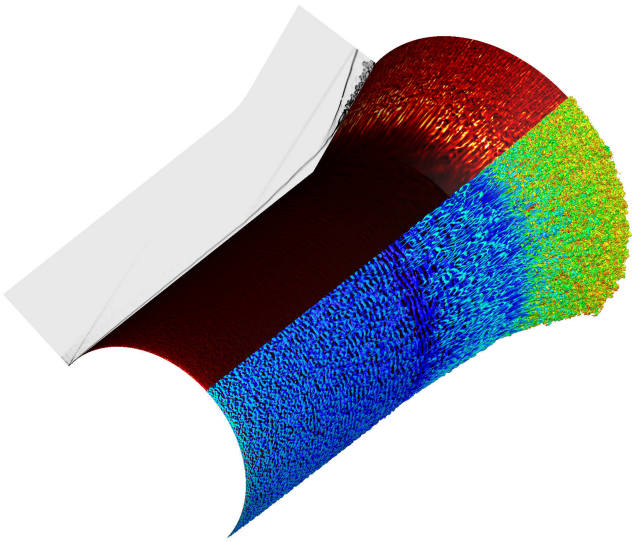

Fig. 5 Illustration of the DNS: isosurface of Q criterion colored by density, heat-fluxes map at the wall and numerical Schlieren visualization (from an instantaneous snapshot).

Lugrin et al. [23]. White noise is injected in the density field in a plane ($j \in [0, 60]$ for the wall normal direction and $k \in [0, 1800]$ for the azimuthal direction) four cells downstream of the inlet boundary condition :

$$\rho'[j,k] = \rho[j,k](1 + Ar_n[j,k]), \tag{1}$$

with ρ the density, r_n a random number which has been Gaussian filtered (kernel spanning over 8 cells) to suppress the very-low wavelength oscillation. The amplitude A is the only free parameter of the noise. The noise is updated every 15 iterations.

3. Technische Universität München

DNS were performed to numerically investigate both University of Arizona and ONERA experimental geometries of the hollow cylinder-flare configuration aiming at assessing the effect of different noise levels on the corner-induced

SWBLI. For the calculations, the Navier–Stokes Multi Block (NSMB, [35]) solver, a finite-volume FORTRAN-written code successfully tested and employed in various hypersonic applications [36–38], was used. The numerical simulations were performed on structured-mesh grids employing a spatial low-dissipation, fourth-order central scheme, together with a second-order Jameson-Schmidt-Turkel (JST) dissipation scheme to deal with flow discontinuities such as the separation and reattachment shocks. A third-order Runge-Kutta scheme was employed for the time discretization, in order to accurately capture the flow-transition phenomenon. The grid characteristics and freestream-inflow conditions have been specialized for the two cases under investigation.

Regarding the experiment at University of Arizona, the conditions of the LT5 Run 1 [10] have been reproduced: $M_\infty = 4.82$, $Re_L = 1.1 \times 10^6$, $T_\infty^\circ \simeq 433K$, $p_\infty^\circ \simeq 3.80 \times 10^5 Pa$ with $T_\infty^\circ = 305K$. The computational grid is composed of $5000 \times 391 \times 81$ points and covers an azimuthal span of 8.4° with axisymmetric lateral boundary conditions. At the outflow and upper part of the domain, characteristic variables with extrapolation in space are imposed to avoid undesired wave reflections. No-slip boundaries are prescribed at the wall, while Dirichlet conditions with freestream values are imposed at the inflow plane.

A similar numerical setup is employed to replicate the R2Ch Run 1 [8] investigated at ONERA with freestream conditions: $M_\infty = 5$, $Re_L = 1.1 \times 10^6$, $T_\infty^\circ \simeq 547K$, $p_\infty^\circ \simeq 4.14 \times 10^5 Pa$ with $T_\infty^\circ = 290K$. Due to the larger HCF model, the computational grid for this case is composed of $6500 \times 431 \times 81$ points, spanning over 15° in azimuthal direction. In both cases, a sharp leading edge is employed. On top of the freestream values, pseudo-random noise is prescribed at the inflow plane in the form of pressure fluctuations to be added to freestream value according to $p = p_\infty + p'(y, z, t)$ in order to take into account noise radiated from the nozzle-wall boundary layers, where:

$$p'(y, z, t) = A^{TU} \cdot p_\infty \cdot \sum_{(i,j)} r_i(y, z) \cdot sin(2\pi f_j t). \tag{2}$$

The parameter A^{TU} controls the overall amplitude of the noise field, while $r_i(y, z)$ is a random-number distribution. The pseudo-random white noise is obtained by randomly combining the numbers $r_i(y, z)$ and eleven frequencies f_j from the equispaced spectrum $[5, 200]kHz$. Different values of the controlling parameter A^{TU} are chosen in order to tune the mean turbulence level in the freestream for the two investigated setups (figure 6).

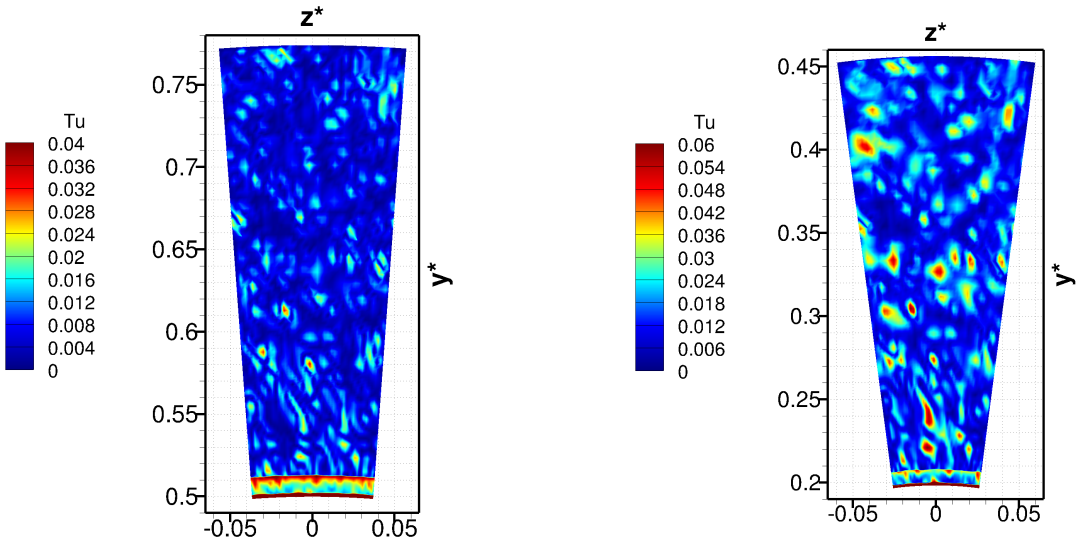

(a) University of Arizona, case with $A^{TU} = 0.010$

(b) ONERA, case with $A^{TU} = 0.020$

Fig. 6 Noise distribution on a vertical plane at $x = 0.08m$ from the inflow.

III. Comparison of Results

A. Scaling of Mean SBLIs

Threadgill et al. [10] reported initial high-Reynolds number results from IR measurements (at $12 < \mathrm{Re}_L/\times 10^5 < 37$. Figure 7 shows a 3D rendering of the extracted typical surface Stanton numbers, as a function of Reynolds number. Surface distributions show strong uniformity around the azimuth, providing confidence that angle of attack/yaw effects are minimal. Results at each Reynolds number show qualitative agreement, albeit with feature locations scaled accordingly. A dominant Stanton number peak is observed on the flare surface, which is associated with reattachment of the separation bubble present at the base of the flare. The location of this peak moves toward the flare base at higher Reynolds numbers, indicating a smaller interaction is present. This scaling agrees with the scaling of turbulent SBLIs [39] which show that the separation length remains quasi-constant when normalized by the incoming boundary layer height. In this case, higher-Reynolds number will induce a smaller boundary layer, and is thus consistent with a smaller bubble (*i.e.*, upstream translation of reattachment for higher Reynolds numbers).

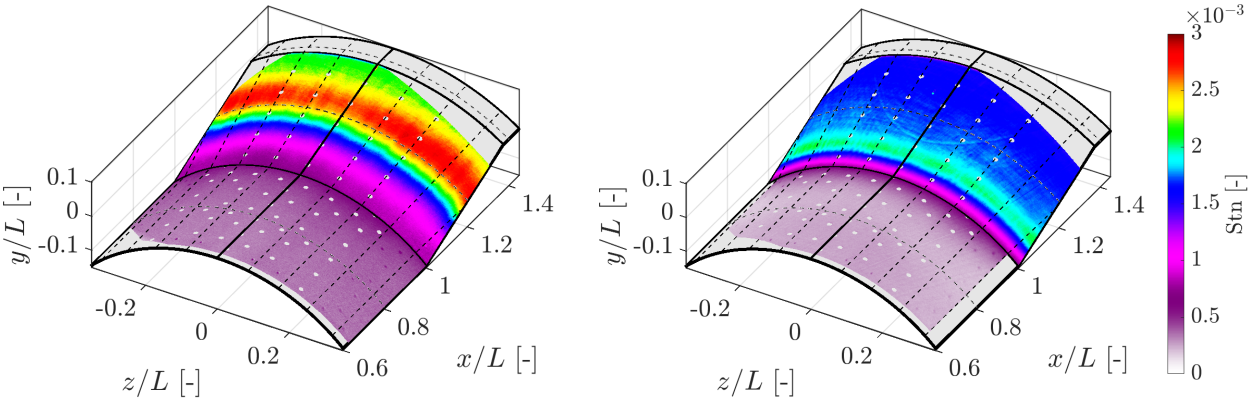

(a) $\mathrm{Re}_L = 1.16 \times 10^6$ (b) $\mathrm{Re}_L = 3.70 \times 10^6$

Fig. 7 Stanton numbers for lower and upper Reynolds numbers[10], plotted in 3D. Dashed black streamwise lines indicate 10° increments of azimuth.

Similar Stanton number data was also published by Lugrin et al.[8] for the HCF tested in R2Ch at a lower Reynolds number range ($4 < \mathrm{Re}_L/\times 10^5 < 11$), shown in Figure 8. Similar topologies are observed in both cases, despite the differences in Reynolds number ranges. A peak is observed on the flare surface, which also moves towards the base as the Reynolds number is increased. This peak in Stanton number is largely uniform in azimuth, with superimposed quasi-regular spaced longitudinal streaks. These streaks have been reported in both datasets and is the subject of ongoing research; however, it is beyond the scope of the present paper.

1. Combined

Results for mean azimuthal Stanton number distributions are shown in Figure 9, enabling a direct comparison between the two different experimental facilities. Despite testing at different Reynolds numbers, the extremes of each facility tests overlaps at $\mathrm{Re}_L \approx 11 \times 10^5$. However, despite this agreement, the location of peak heating is significantly further downstream in data from LT5, as opposed to R2Ch. This difference is highlighted in the figure as $\Delta x/L = 0.105$. It should be noted that SBLIs have been well-characterized to scale with respect to the location of the inviscid pressure rise (for a given SBLI state), *i.e.* the flare base for this configuration at x/L. When rescaled relative to this position, the significance of the discrepancy is more apparent, with the LT5 peak located approximately twice as far downstream of the flare base as the data from R2Ch.

This difference across the Reynolds number range is further elucidated in Figure 10 which plots the peak location *vs.* Reynolds number for both data sets. A scaling factor of $1/1.9$ is applied to the LT5 data to show the magnitude of this difference and demonstrates a smooth continuous trend when applied. The magnitude of this discrepancy is puzzling, particularly since each of these configurations is nominally similar, with minimal differences in: Mach number (−3.7%), Reynolds number (+5.5%) and flare angle (0.0%), where data from R2Ch are used as the reference value in each comparison.

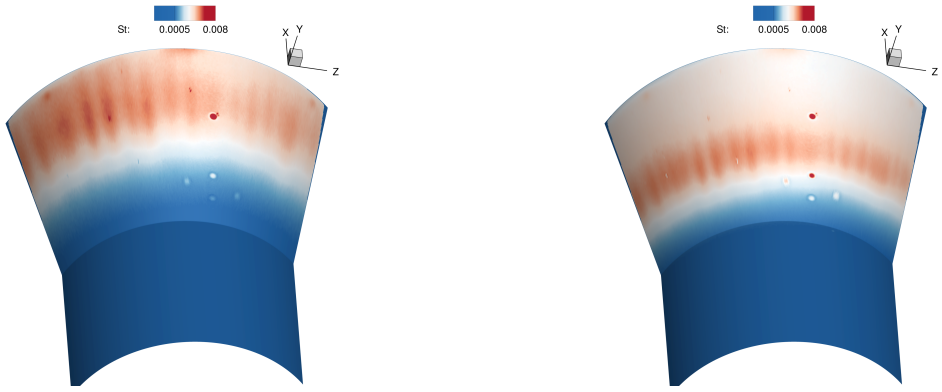

(a) $\mathrm{Re}_L = 4 \times 10^5$ (b) $\mathrm{Re}_L = 7 \times 10^5$

Fig. 8 Stanton numbers for two Reynolds numbers, plotted in 3D. Reprinted from Lugrin et al. [8]

The cause of this discrepancy is of great interest since similar flow topologies would be expected considering the closeness of the tested configurations. Numerous factors may be relevant to this characterization and are considered below with respect to their influence on interaction scaling:

- Boundary layer scaling: variation in boundary layer thickness upstream of the interaction due to differences in Mach number and T_{aw}/T_w acting to scale the SBLI with this length scale.
- 3D effects: difference in interaction strength due to 3D relief effects of dissimilar normalized base diameters D/L. Despite matching geometric flare angles, imposed inviscid pressure rise may differ.
- Leading edge sharpness: variation in boundary layer thickness due to dissimilar leading edge sharpness acting to scale the SBLI. Also, non-sharp leading edge may attenuate certain instabilities, affecting transitional behavior.
- Noise environment: Difference in noise environment for each facility and its effect when forcing the tested configuration.

Each of these influences is probed and discussed in the following subsections to obtain a measure of the relative significance of each effect. The aim is to quantify the respective influence and see if the 1.9 scaling (*i.e.*+90%) can be accounted for through consideration of each. The scope of these discussions is focused on relevance to the experimentally tested configurations shown above.

B. Boundary Layer Growth Effect

Despite similar nominal test conditions, the experiments conducted at UArizona and ONERA exhibit small differences in freestream Mach number and wall-temperature conditions. These effects are known to influence the growth of the boundary layer so it is important to quantify this effect in this study to assess the relative significance. For simplicity, these effects are considered with reference to an idealized similarity solution for a laminar boundary layer, as shown in Figure 11 for each facility. Even when normalized by model length and Reynolds number, it is clear that the respective boundary layers differ, while maintaining a significant degree of similarity in all but the temperature and density profiles. The relatively cold walls of the ONERA tests ($T_w/T_{aw} = 0.61$, *vs.* $T_w/T_{aw} = 0.79$ at UArizona) act to lessen the boundary layer growth by increasing flow density near the wall.

Quantifying this effect is highly dependent on the boundary layer thickness threshold employed. For completeness, Table 3 shows normalized thicknesses assessed using a range of these approaches. Turbulent SBLIs have been demonstrated to scale with the displacement thickness[39, 40] δ_1, but experimental studies frequently report threshold-based values due to the difficulties of integration throughout the entire boundary layer. Since the application of these thresholds varies, Table 3 shows an exhaustive list of potential values. Two definitions rely on enthalpy-based thresholds and are written with respect to T_0, assuming an ideal gas: i) the location of max entropy at the overshoot on the outer part of the region identified as the lowest height with zero gradient in the total temperature profile [41], $\delta_{(dT_0/dy=0)}$; and ii) a threshold-based approach for the largest height when the total temperature returns to within 0.3% of the freestream conditions [42], $\delta_{|T_0/T_{0_\infty}-1|=0.003}$.

Regardless, the degree of variation through these definitions is relatively small, with all predicting larger normalized boundary layer at UArizona by +5.9% to +14.0%, which is far from the difference of +90% to account for the differences

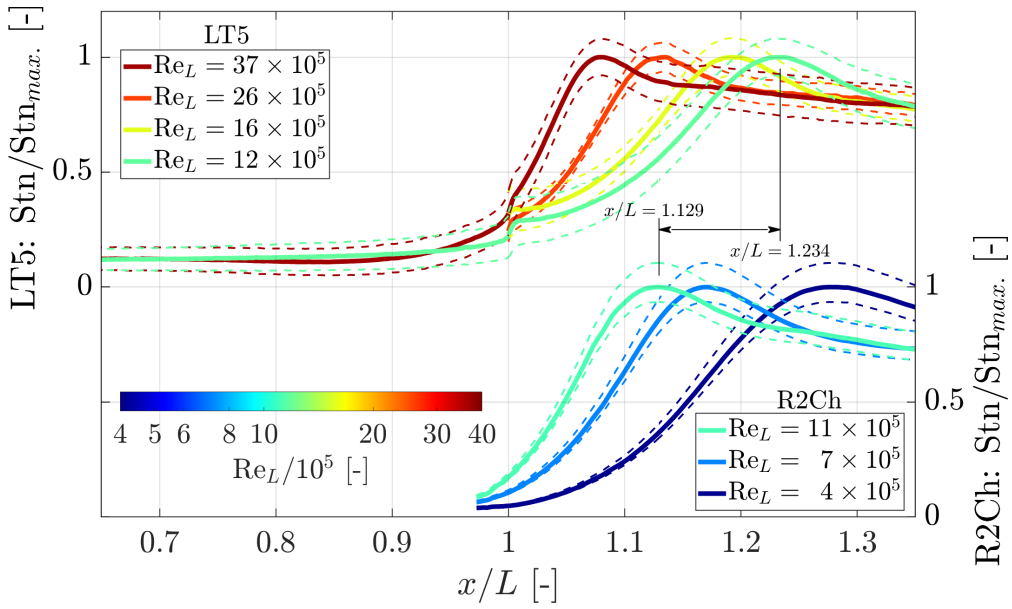

Fig. 9 Mean Stanton number profiles from LT5 and R2Ch (averaged in azimuth and time), across a range of Reynolds numbers Re_L. Dashed lines indicate uncertainties in each dataset. Differences in reattachment peak location for similar Reynolds numbers are highlighted ($\mathrm{Re}_L \approx 11 \times 10^5$).

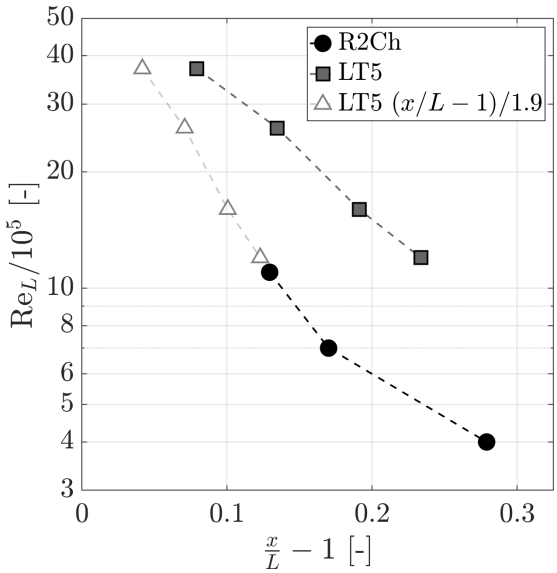

Fig. 10 Comparison of reattachment Stanton number peak locations [8, 10]. An approximate scaling of $1/1.9$ is also applied to data from LT5 for reference.

in experimental data. Momentum thickness δ_2, energy thickness δ_3, and sonic line height $\delta_{(M=1)}$ are shown in the table for completeness, but are not considered relevant for SBLI scaling.

C. Influence of 3D Relief

The imposed inviscid pressure rise is acknowledged to be one of the principal scaling parameters that drive the length-scales of SBLIs [1, 39, 40, 43]. As a result, considerable effort was made in matching parameters between the experiments in LT5 and R2Ch as much as possible. As a result, both tests were conducted in $M_\infty \approx 5$ flow, with nominally sharp leading edges, matching Reynolds numbers of $\mathrm{Re}_L \approx 11 \times 10^5$, and equal flow deflection at the flare

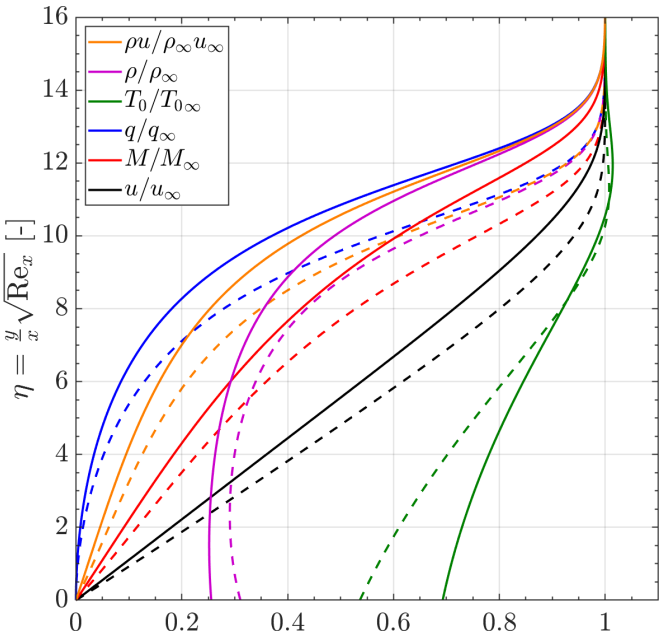

Fig. 11 Comparison of similarity solution boundary layer profiles between LT5 (solid) and R2Ch (dashed).

surface. However, two parameters remain which lead to discrepancies in the inviscid pressure rise and will be discussed here.

A subtle difference in the observed Mach number of each facility ($M_\infty = 4.82$ for LT5, $M_\infty 5.0$ for R2Ch) affects the 2D pressure rise from an oblique shock with a common $\theta = 15°$ deflection. As a result, simple thin-shock theory shows that the inviscid pressure coefficient for LT5 is 1.6% greater than for R2Ch, giving a slight increase to the expected SBLI length scale.

Another difference between the two experimental configurations relates to the cylinder diameters. Until now, most consideration has been placed on the length of the cylinder with the understanding that the diameter is sufficiently large that it is of secondary significance. For reference, the cylinder circumference normalized by the similarity solution boundary layer thicknesses at the flare base (assuming no SBLI is present) is $C/\delta_{99} = 267$ (for LT5) and $C/\delta_{99} = 149$ (for R2Ch). Since flow is parallel to the cylinder axis, growth is expected to be equivalent to the 2D case and unaffected by the diameter parameter. However, the same cannot be said on the flare itself. Similarly to a cone, the flow moving across the flare will experience a 3D relief effect that will lessen the effective pressure rise when compared to a fully 2D

Thickness definition	$\frac{\delta}{x}\sqrt{\mathrm{Re}_x}$		$\frac{\delta_{LT5}}{\delta_{R2Ch}}$	
	LT5	R2Ch		
$\delta_{(u/u_\infty=0.99)}$	12.682	11.479	1.105	Velocity-layer
$\delta_{(\rho u/\rho_\infty u_\infty=0.99)}$	14.460	13.212	1.094	
$\delta_{(dT_0/dy=0)}$	11.937	11.270	1.059	Enthalpy-layer
$\delta_{\left(\lvert T_0/T_{0_\infty}-1\rvert=.003\right)}$	13.950	12.568	1.110	
$\delta_1 = \delta^*$	9.602	8.423	1.140	
$\delta_2 = \theta$	0.642	0.633	1.014	Integral parameters
$\delta_3 = \delta^{**}$	1.342	1.547	0.870	
$\delta_{(M=1)}$	4.457	3.508	1.271	Sonic layer

Table 3 Comparison of various similarity solution laminar boundary layer thickness definitions across each facility (LT5: $M_\infty = 4.82$, $T_0 = 433$, $T_w = 300$; R2Ch: $M_\infty = 5.00$, $T_0 = 550$, $T_w = 295$).

flow, despite matching surface deflection angles. The limits of this effect can be estimated by taking diameter tending towards zero with the 15° flare becoming a cone of the same angle. In this configuration (assuming $M_\infty = 4.82$), the inviscid pressure coefficients are 0.129 and 0.220, for the cone and 2D flows, respectively. The normalized cylinder diameters in the experimental models are $D/L = 1.00$ (LT5) and $D/L = 0.52$ (R2Ch), so one would expect the pressure rise in R2Ch to be slightly weaker for the same incoming Mach number (assumed $M_\infty = 4.82$ in this comparison, to isolate effect of diameter). Figure 12 shows the comparason of pressure coefficient distributions over the cylinder/flare surface. It should be noted that both cases have a 1 mm radius applied at the base of the flare during grid generation, leading to the slightly smoothed values at $x/L \approx 1$. Regardless, the difference in pressure coefficient is shown to be minimal when varying the normalized base diameter alone, with the larger diameter (matching LT5) resulting in a 1.3% higher pressure coefficient than the smaller diameter (matching R2Ch).

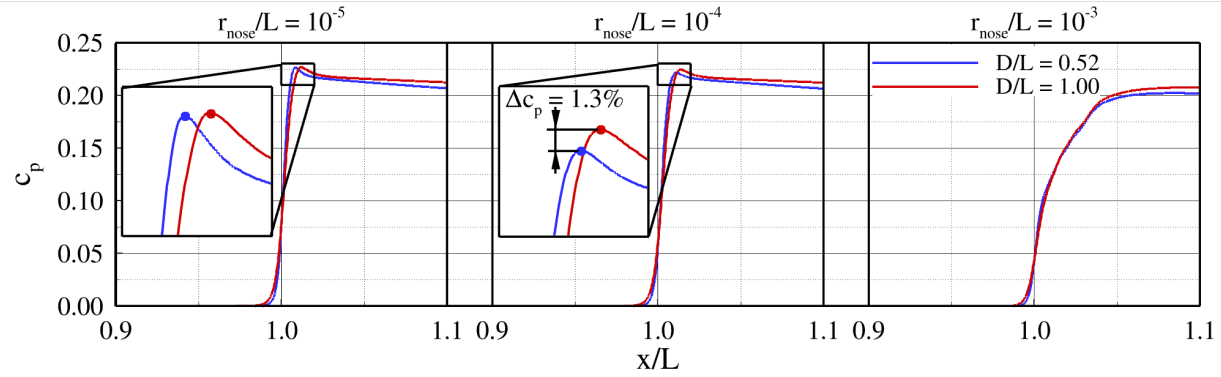

Fig. 12 Simulations of baseflows to assess impact of normalized cylinder diameter (D/L) across a range of normalized nose bluntnesses (r_{nose}/L), $M_\infty = 4.82$, $\theta = 15°$

Combined, these effects of small differences in Mach number and cylinder diameters have been assessed to account for +1.6% and +1.3%, respectively (when comparing LT5 to R2Ch), yielding a net baseline interaction strength in LT5 to be 2.9% higher.

Another significant observation from Figure 12 is the effect of normalized nose bluntness in affecting the inviscid pressure coefficient between each case. For reference, the experimental nose bluntnesses were $r_{nose}/L = 5.7 \times 10^{-4}$ and 1.1×10^{-4}, for LT5 and R2Ch respectively. As a result, the pressures near the base of the flare ($1.00 < x < 1.05$) are lower for the blunter case, before recovering to similar values further downstream for $x > 1.05$. The effect of nose bluntness will be considered in the following subsection.

D. Effect of Leading Edge Radius

For experiments, a test model will always have a finite leading edge radius. Very small leading-edge radii can result in a substantial reduction of growth rates and N-factors of both first and second mode instability waves and therefore can have a profound impact on where transition will occur (see Haas et al. [44]). Consequently, for the numerical investigations it is crucial to match the leading-edge bluntness of the experiments as closely as possible to enable meaningful comparisons of the computational results with experimental measurements.

Experiments by Chuvakhov et al. [45] indicated that the leading-edge radius of the hollow cylinder flare geometry has a non-negligible effect on the separated region at a Mach number of 8 for various unit Reynolds numbers. Axisymmetric calculations for the hollow cylinder flare geometries used for the experiments at the UA (Section II.A.1) and ONERA (Section II.A.2) using CFD++ have indicated a similar trend of the separation length (L_s) as a function of the leading-edge radius (r_{nose}). The calculations for the UA geometry were carried out for $M = 4.82$, $Re_L = 12 \times 10^5$ and $T_{\text{wall}} = 300$ K and the calculations for the ONERA geometry for $M = 5.0$, $Re_L = 19 \times 10^5$ and $T_{\text{wall}} = 290$ K (conditions for the simulations by Lugrin et al. [23]). The Mach number contours for three different leading-edge radii for the UA geometry and flow conditions are provided in Fig. 13. The $u/U_\infty = 0$ iso-contour lines are also shown in Fig. 13 to indicate the topology of the separation bubble. When increasing the leading edge radius from $r_{\text{nose}} = 1 \times 10^{-6}$ m to $r_{\text{nose}} = 100 \times 10^{-6}$ m the separation location moves upstream while the reattachment moves in the downstream direction, thus significantly increasing the separation length (Fig. 13). Further increasing the leading edge radius to $r_{\text{nose}} = 5000 \times 10^{-6}$ m shows that these trends are reversed and the separation location is shifting downstream while

the reattachment location moves upstream (Fig. 13). This is consistent with the trends reported by Chuvakhov et al. [45]. The effect of the leading-edge bluntness on the separation length (L_{sep} and the separation (x_{sep}) and reattachment (x_{rea}) locations are provided in Fig. 14 for both the UA and the ONERA geometries and flow conditions. The results in Fig. 14(a) show that in both cases the separation length normalized with the distance of the ramp to the leading edge first increases and reaches a maximum around $r_{nose}/L \approx 0.003$ before dropping rapidly for increasing values of r_{nose}/L. The reported r_{nose}/L of each experiment are marked by vertical dashed lines in Fig. 14(a). The dependency of the separation and reattachment locations on the leading-edge radius is provided in Fig. 14(b). It indicates that the separation location first moves upstream until it reaches a minimum near r_{nose}/L between 0.001 and 0.002 and then shifts in the downstream direction again. The trend for the reattachment location is the opposite (Fig. 14(b)). The maximum for the reattachment location is obtained for $r_{nose}/L \approx 0.01$. The underlying physics that govern why separation location increases again for increasing leading-edge radii is currently not yet understood. The impact of the different Re_L values have on the difference in separation length as a function of the nose radius between the UA and ONERA geometries (see Fig. 14(a)) is subject to future investigations.

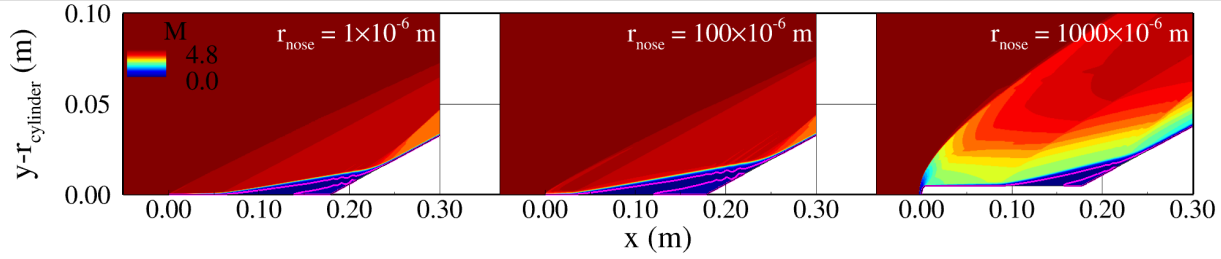

Fig. 13 Mach number contours and isocontour lines for $u/U_\infty = 0$ for increasing leading edge radius (from left to right). Aspect ratio of axes is x/y = 1/2.

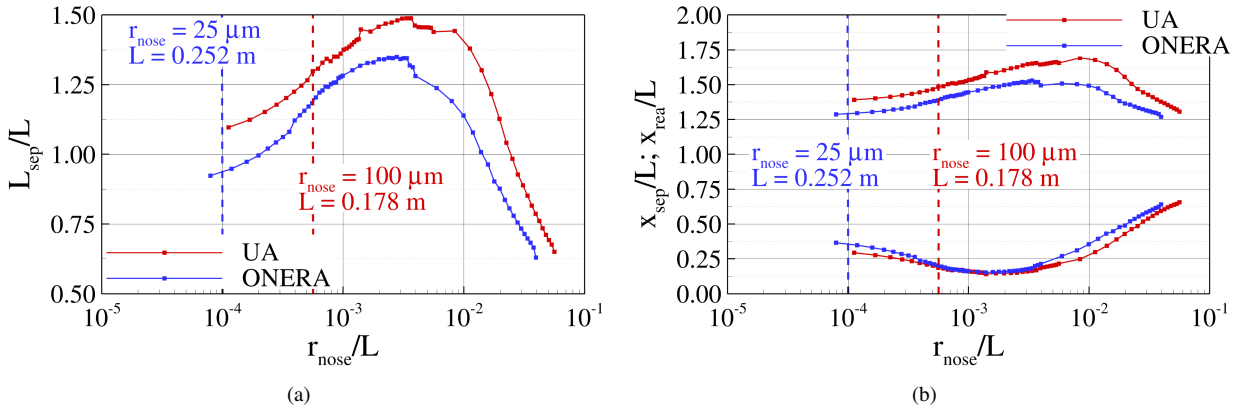

Fig. 14 Length of separation bubble (L_{sep}) normalized by the ramp location (a), and separation (x_{sep}) and reattachment (x_{rea}) location normalized by the ramp location (b) as a function of the normalized leading edge radius (r_{nose}/L).

E. Effect of Freestream Noise

1. Simulated Noise

Previous numerical studies from ONERA [23] have shown that the level of free-stream noise has an impact on the size of the separated region on HCF configurations in hypersonic flow as long as the flow is transitional at reattachment. Figure 15 illustrates this by showing two instantaneous numerical pseudo Schlieren images for the same flow conditions but different level of free-stream noise. In order to optimize the amplitude A (see Equation 1) of the noise level to

match the experiment, the error on the recirculation region size is chosen as the objective function to minimize. This choice is motivated by two reasons: first, Lugrin et al. [23] showed that it is very sensitive to the amplitude of the injected perturbation for an almost similar case (slightly higher Reynolds number). This is illustrated in Figure 15, which presents a numerical Schlieren image for the same case with different level of free-stream noises, showing that different perturbation levels strongly influence the bubble size. The exact phenomenon behind this strong coupling is still not completely known, but both experimental and numerical mean flow observation show that transition never happen in the mixing layer, but either at or downstream of reattachment and that the size of the separated region is directly correlated with the transition process. As such, an increase in free-stream noise level, or Reynolds number, that lead to faster transition causes a shrinking of the bubble size.

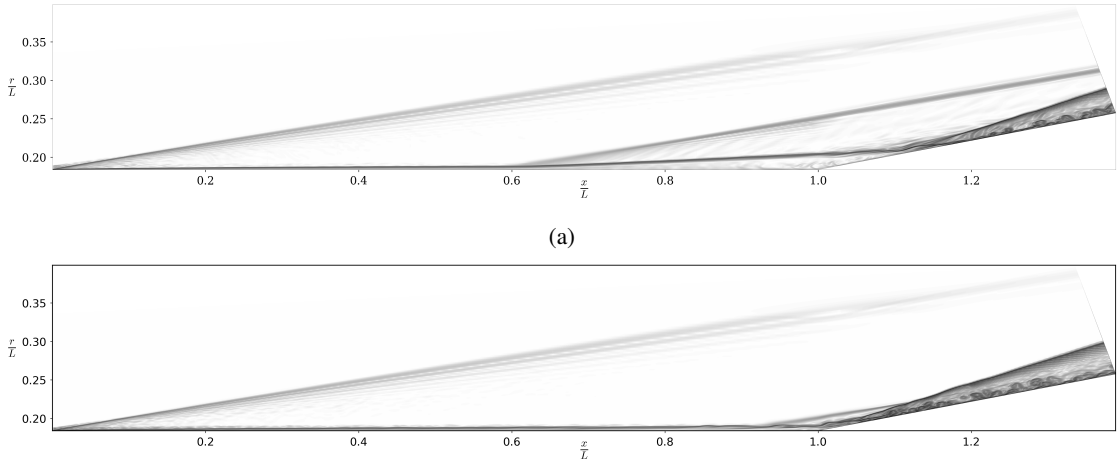

(a)

(b)

Fig. 15 Numerical pseudo Schlieren visualization for the same conditions but varying level of noise (a) low level, (b) high level, showing the impact on the separated region size.

The effect of freestream noise on the separation length it is very well described in the experiments thanks to the high density of pressure taps along the cylinder and the flare (50). As such, the level of noise can be chosen such that it leads to a correct reproduction of the mean size of the separated region. A simple optimization of the noise amplitude is conducted by computing mean-flow of the DNS for different level of noise, leading to an optimal amplitude of $A = 0.005375$.

Figure 16 presents the time-averaged results from both the simulations and the R2Ch experiment. With the optimized noise level, the bubble size is very accurately reproduced, with correct positions of the separation (first increase in pressure from $\frac{P}{P_\infty} = 1$ to roughly 1.5) and reattachment point (second increase in pressure after the plateau at 1.5). Two other amplitudes of injected noise, one higher and one lower, are also displayed to illustrate the strong impact of the noise on the mean separation size. For this Reynolds number range, the flow transition takes place at the reattachment point [23], therefore the correct match of the bubble topology means that the transition location is correctly predicted by the simulation.

Figure 17 (a) presents a comparison of pressure power-spectral densities for a sensor located inside the recirculation region upstream of the transition point. First, the spectra match for the very low frequency content. For frequencies higher than 2 kHz, the DNS spectrum starts to depart from the experimental one, as it displays lower levels of energy. Then for frequencies higher than roughly 30 kHz the DNS energetic content increases and becomes greater than the experimental value. One has to be careful when interpreting the results around $80 - 100$ kHz as the huge peak in the experimental spectrum is due to the resonance of the sensor membrane. The main information that we can get from figure 17 (a) is that the DNS seems to contain more energetic structures at higher frequencies, while the experiments display a higher level of energy for low frequencies. The most amplified instabilities in the DNS and experiments are not matching, nor the general shape of the spectrum.

Figure 17 (b) presents the same results for sensors located on the flare, in a turbulent region of the flow, note that for this location, two sensors are available, including a PCB sensor which allows to interpret the results from 10 kHz up to 300 kHz. Note that for high-frequency content (higher than $20 - 30$ kHz), the PCB sensor is more accurate than the

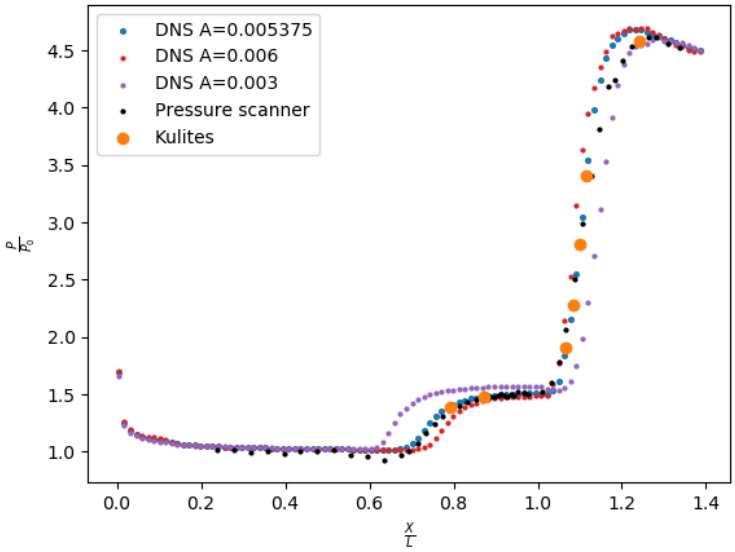

Fig. 16 Wall pressure distribution for different amplitudes of injected white noise, showing the impact of the noise on the separated region size.

Kulite sensor. This figure shows that downstream of the transition location, the DNS results are exactly similar to the experimental in the whole frequency range that can be experimentally measured. While this does not bring information on whether the transition process is the same in the simulation and the experiments, it is still an important result as it shows that even if the instabilities upstream of the transition point are not matching, the fully turbulent spectrum downstream of the transition point can be accurately reproduced numerically.

The results of figure 17 (b) should also be kept in mind while interpreting the results shown in figure 17 (a) as the signal from the Kulite sensor decreases for frequencies higher than 10 kHz. Keeping that limitation in mind and going back to the results of figure 17 (a) one can conclude that the white noise injected in the simulation is lacking low frequency content and may be biased towards high-frequencies. The lack of spatial length-scale information also is a source of uncertainty towards the potential matching of experimental to simulation results based on the available frequency spectra of the measurements.

At the Technical University of Munich, numerical simulations were performed in order to compare the two experimental runs at $Re_L \simeq 1.1 \times 10^6$ investigated at the University of Arizona and ONERA, respectively. The simulations were performed with similar values of the noise-amplitude parameter A. Starting with the setup employed in the experiments at the University of Arizona, the DNS performed at TUM focused on two background-noise levels, namely for the amplitude-parameter values $A_1^{TU} = 0.005$ and $A_2^{TU} = 0.010$. An overview of the main results is given in figures 18, 19a, 20 and 21.

The noise intensity has a noticeable effect on the separation-bubble size. Namely, a higher noise level corresponds to a delayed separation and hence a smaller recirculation region, confirming what was observed in the other numerical experiments presented in this work. Figure 18 shows the instantaneous density field obtained under the two different noise conditions A_1^{TU} and A_2^{TU} along a streamwise slice. For the lower-noise level A_1^{TU}, the boundary layer detaches at $x_s^* \simeq 0.624$. By doubling the disturbance intensity, instead, the separation point moves downstream to $x_s^* \simeq 0.759$, resulting in a smaller bubble. The different separation length can be also deduced by figure 20a, showing the spanwise- and time-averaged pressure distribution at the surface of the cylinder-flare configuration.

In both cases A_1^{TU} and A_2^{TU}, the detached shear layer is transitional on the flare, which is also visible from the Stanton-number distribution at reattachment, with the A_2^{TU} case shown in figure 19a. Opposite to the separation-bubble length, the heat flux at reattachment increases with the background noise. In particular, the peak detected at reattachment becomes stronger. This is visible in figure 20b, which shows the Stanton-number distribution at the wall averaged over a time window of $0.4ms$. The streamwise location of the main peak obtained for the noise-amplitude parameter A_1^{TU} is the same observed in the experiment at University of Arizona, suggesting that also the length of the separation bubble from the simulation would match the experimental one. The magnitude of the DNS heat-flux is, however, twice as high

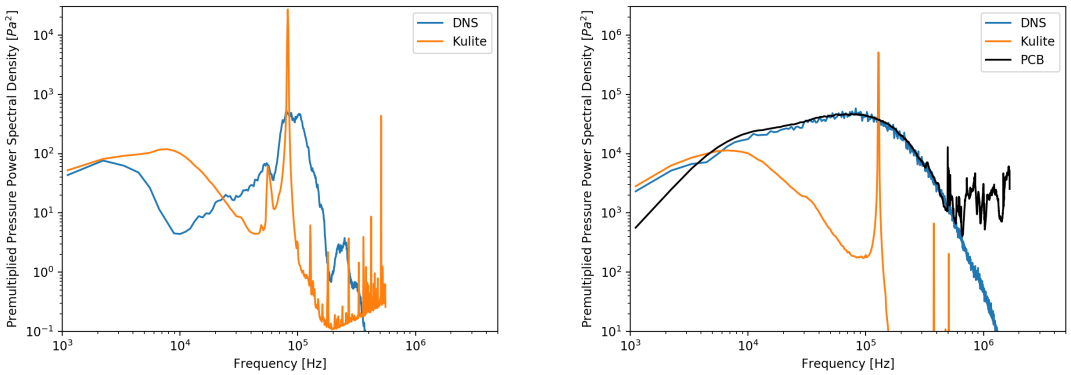

(a) Inside the separated region ($x/L = 0.87$). (b) After reattachment ($x/L = 1.1$).

Fig. 17 Comparison of the numerical and experimental pressure power spectral densities. Note the resonance of the Kulite sensor just before 100 kHz, showing the lack of low-frequency spectral content in the DNS.

as that of the experiment.

By averaging the unsteady flow-field over time, hot streaks are revealed on the flare downstream of reattachment, as shown in figure 21. Under low-noise conditions, four distinct streaks develop in azimuthal direction. By increasing the freestream noise, the streaks shorten and become stronger, with two of them almost merging into a single one.

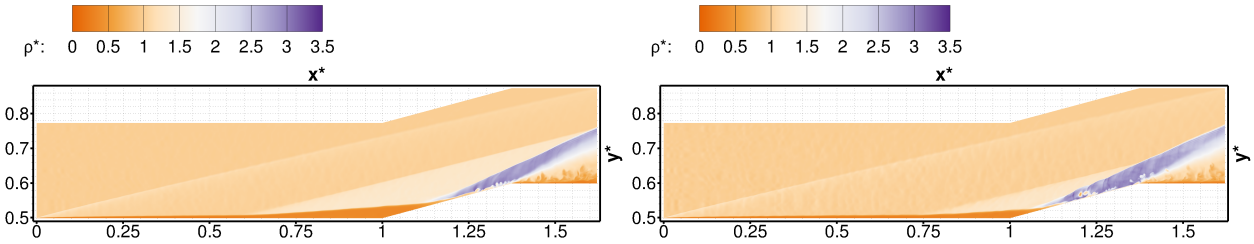

(a) Lower-noise environment ($A_1^{TU} = 0.005$). (b) Higher-noise environment ($A_2^{TU} = 0.010$).

Fig. 18 University of Arizona setup, instantaneous snapshots of the density field along a streamwise slice.

Similar results were obtained also for the ONERA configuration, for which three different noise levels were investigated, corresponding to the amplitude parameters $A_1^{TU} = 0.005$, $A_2^{TU} = 0.010$ and $A_3^{TU} = 0.020$. By increasing the freestream noise, the recirculation bubble shrinks due to the delayed boundary-layer separation upstream of the flare. The length of the bubble obtained for the lowest noise amplitude A_1^{TU} almost matches the one measured in the wind-tunnel investigation ($x_s^* \simeq 0.740$, figure 20a). At this noise level, however, the SWBLI interaction is not fully transitional as found in the experiments at ONERA or in the University of Arizona simulations, and only towards the end of the flare some breakdown spots are detected. Doubling the amplitude to $A_2^{TU} = 0.010$, the interaction starts to show a transitional behavior on the flare, with the flow breaking down at reattachment (figure 19b). For A_2^{TU} case, the separation location moves downstream to $x_s^* \simeq 0.841$, while by further doubling the amplitude to $A_3^{TU} = 0.020$, the boundary layer separates at $x_s^* \simeq 0.865$.

As expected, the Stanton-number peak on the flare becomes stronger as the noise in the freestream increases. Similar to what was observed for the University of Arizona configuration, the hot streaks at the wall characterizing the mean flow are also affected by the wind-tunnel noise and tend to shorten for higher values of the amplitude parameter A^{TU} (figure 22).

Comparing the two experimental setups in terms of normalized spanwise width, the streaks have comparable size

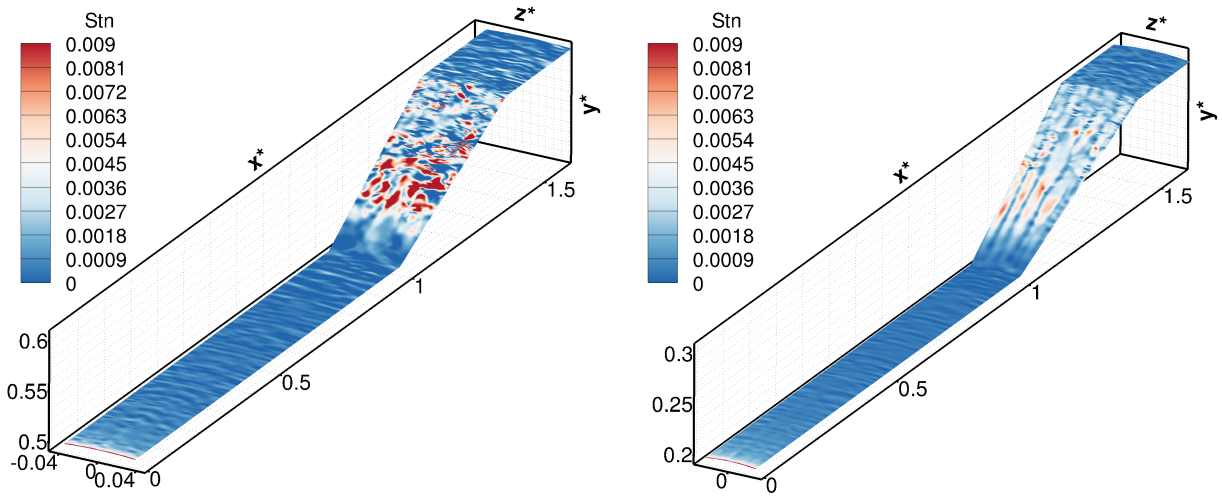

(a) University of Arizona setup.

(b) ONERA setup.

Fig. 19 Instantaneous snapshots of the Stanton-number distribution at the wall for $A_2^{TU} = 0.010$.

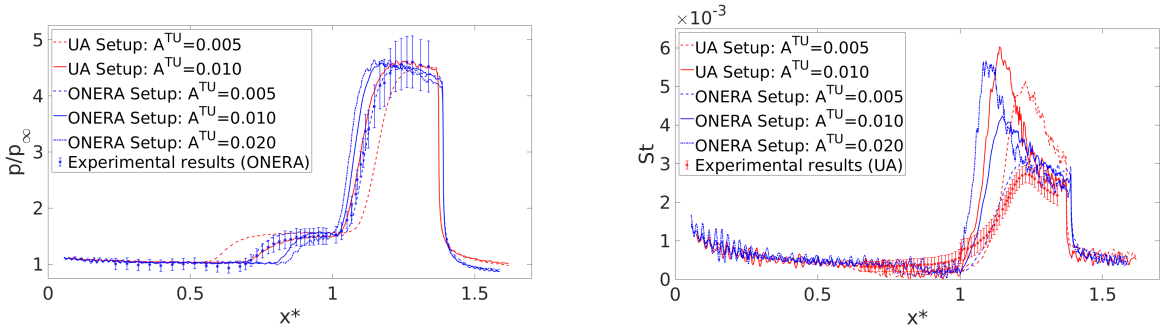

(a) Wall-pressure distribution.

(b) Stanton-number distribution.

Fig. 20 Spanwise- and time-averaged wall-coefficient distributions: UA in red, ONERA in blue.

in both investigated configurations. However, there is a shift in the noise-parameter value, since lower disturbance amplitudes are needed to trigger a transitional interaction when considering the configuration investigated at the University of Arizona (see figure 19).

DNS for which random disturbances are introduced at the inflow of the computational domain are carried out at the University of Arizona. For these simulations the azimuthal width of the computational domain is varied in order to investigate the influence of domain confinement (as shown in Fig. 23). A semi-cylindrical leading edge is used in the simulations, using a nose radius of $r_{\text{nose}} = 100\mu$m consistent with experiments (see Section II.A.1). In the transition simulations (step 3, Fig. 4), the inflow boundary of the computational domain is positioned downstream of this leading edge. These simulations are ongoing. However, the interim status is shown in Fig. 23, which depicts the instantaneous pressure disturbances on the surface of the hollow cylinder/flare geometry. Additionally, the instantaneous total density contours are shown in a wall-normal plane, which includes the $u/U_\infty = 0$ isocontour lines.

In both simulation setups with the different azimuthal domain sizes, instabilities are observed in the shear layer. Notably, the emergence of smaller scales in the pressure disturbance contours suggests the onset of transition. This phenomenon is accompanied by an upstream movement of the reattachment point (earlier re-attachment), as discussed above. The next steps involve time-averaging the flow field to determine the time-averaged Stanton numbers on the surface of the hollow cylinder/flare geometry and to quantify the mean flow bubble size. These results will then be compared with the simulation results from TU Munich (Fig. 20).

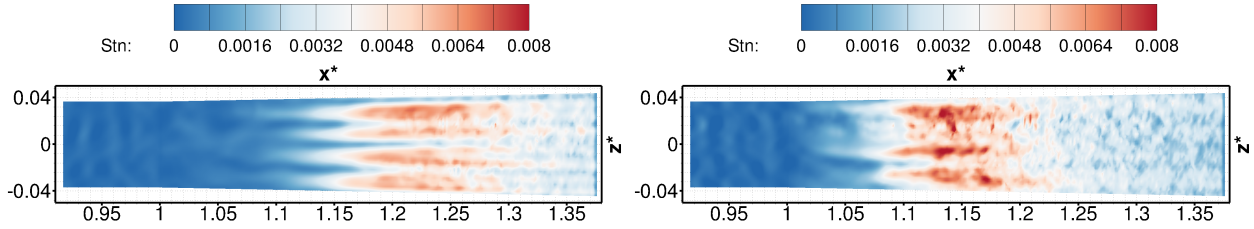

(a) Lower-noise environment ($A_1^{TU} = 0.005$). (b) Higher-noise environment ($A_2^{TU} = 0.010$).

Fig. 21 University of Arizona case, time-averaged Stanton-number distribution on the flare.

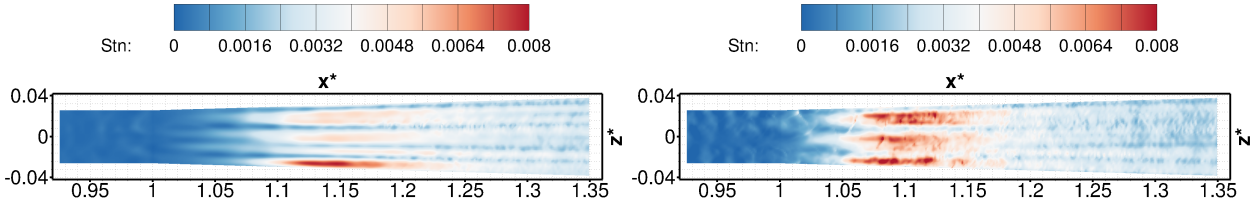

(a) High-noise environment ($A_2^{TU} = 0.010$). (b) High-noise environment ($A_2^{TU} = 0.020$).

Fig. 22 ONERA setup, averaged Stanton-number distribution on the flare.

2. Experimental Observations

Characterization of the respective freestream noise environments has been performed in R2Ch and LT5 using the same exact probe, a sharp right-cone with 5° half-angle[8] (see figure 24). Reynolds number of the data is at similar magnitudes to the HCF configurations, but does differ slightly ($\mathrm{Re}' = 60 \times 10^5\ \mathrm{m}^{-1}$ for LT5 and $\mathrm{Re}' = 75 \times 10^5\ \mathrm{m}^{-1}$ for R2Ch). The probe is instrumented as close to the tip as possible with two pressure transducers, a Kulite (at $x = 90$ mm) and a PCB 132B38 (at $x = 105$ mm), to characterize the spectra across a wide range of frequencies. Spectra from each sensor are combined into a single spectrum using a linear weighting from being 100% Kulite to 100% PCBs between 20 kHz and 40 kHz, respectively. The cone is designed to maintain a shock that is attached and as weak as possible (at Mach 5), giving a measure of noise close to freestream ($p_c/p_\infty = 1.16$ for cone, $p_{02}/p_\infty = 32.7$ for Pitot probe) to reflect the environment conditions driving the receptivity process.

Figure 25 shows power spectral densitys (PSDs) extracted from tests at each facility, with similar Reynolds number based on cylinder length, Re_L. When plotted in log-log form (Figure 25a) the two traces show qualitative similarities, with somewhat flat response at low frequencies with significant high-frequency roll-off. Note, spectra from LT5 is inherently noisy due to the short test duration so a smoothened profile shown has been superimposed on the figures (black spectra). The spectra of R2Ch appears to be shifted to lower-amplitudes but higher frequencies.

Linear Stability Theory (LST) calculations were carried out for the 5° half-angle cone, used for the freestream noise measurements, to characterize behaviors of any resident instability modes that might be skewing the interpretation of these experimental spectra measured from the surface of the cone. Figure 26 shows the N-factors at various frequencies near the locations of the sensors on the cone at $x \approx 100$ mm, plotted across a range of unit Reynolds numbers relevant for the experiments discussed here ($5 \times 10^6 \mathrm{m}^{-1} \leq Re' \leq 10 \times 10^6 \mathrm{m}^{-1}$ in intervals of $\Delta Re' = 1 \times 10^6 \mathrm{m}^{-1}$). No unstable first mode waves were observed for $Re' = 5 \times 10^6$. In addition, no unstable axisymmetric ($k_c = 0$) first modes are obtained in the investigated Reynolds number range. The most amplified first mode waves are oblique (Mack [46]), therefore the N-factors for the first mode are provided at $k_c = 15$ ($\beta_r \approx 1715\mathrm{m}^{-1}$), for which the most unstable first mode waves were observed. A variation of the Reynolds number has a clear effect on the magnitude of N-factors, with values at the further downstream location of the PCB sensor ($x = 105$ mm) being slightly higher. The second mode dominates when analyzing $k_c = 0$ case (Figure 26a and b). Frequencies shift from 400 kHz to 600 kHz across the range of Reynolds numbers from $\mathrm{Re}' = 6 \times 10^6\ \mathrm{m}^{-1}$ to $\mathrm{Re}' = 10\times^6\ \mathrm{m}^{-1}$, with maximum N-factor values of 0.8. At approximately $k_c = 15$ the maximum N-factors are obtained at the sensor locations and the first mode disturbances

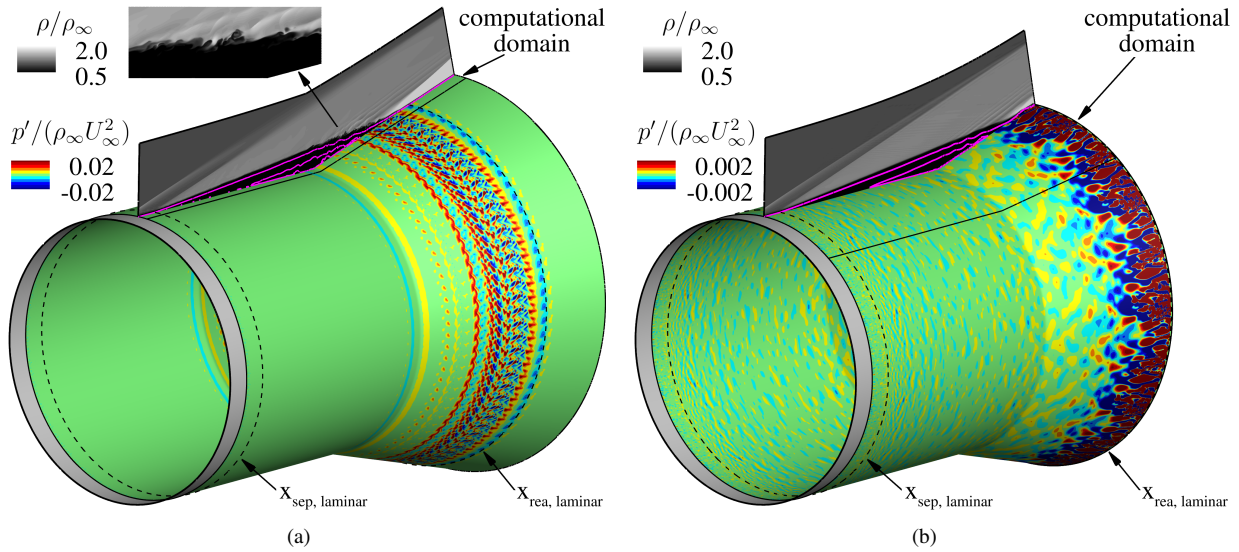

Fig. 23 Instantaneous pressure disturbance contours on the surface of the hollow cylinder flare geometry and instantaneous density contours in a wall-normal plane for an azimuthal domain width of $2\pi/80$ (a), and $2\pi/10$ (b). Note, the data were extended in azimuthal direction for visualization purposes.

are clearly the dominant instability according to LST. Frequencies shift from 60 kHz to 80 kHz across the range of Reynolds numbers from $\mathrm{Re}' = 5 \times 10^6\ \mathrm{m}^{-1}$ to $\mathrm{Re}' = 10\times^6\ \mathrm{m}^{-1}$. At LT5 conditions ($\mathrm{Re}' = 60 \times 10^5\ \mathrm{m}^{-1}$), the first mode N-factor reaches approximately 0.08 at the downstream sensor, with frequency $f \approx 60$ kHz. The second mode has larger N-factors at approximately 0.28, peaking at $f = 410$ kHz. At R2Ch conditions ($\mathrm{Re}' = 75 \times 10^5\ \mathrm{m}^{-1}$), both instabilities show higher N-factors, with the maximum first mode N-factor of approximately 0.16 at the downstream sensor, with frequency $f \approx 65$ kHz. The maximum second mode N-factor is approximately 0.47, peaking at $f = 460$ kHz. The combined Kulite-PCB spectra presented in Figure 25 switches to the PCB-only data at $f > 40$ kHz, so it is the N-factors of Figure 26b and d that would be expected to be present in the spectra presented in Figure 25. The lack of additional energy at the first mode frequencies is clearly evident in Figure 25a. Data at the expected second mode frequency is dominated by the noise floor and is not well-resolved in the spectra. Both spectra show smooth, continuous profiles at frequencies below 200 kHz, without appreciable signs of instabilities present. This provides confidence that the spectra observed are physically relevant to characterization of the freestream and not biased by the linearly amplified disturbance waves on the cone probe.

The pre-multiplied form of the freestream PSDs is shown in Figure 25b to assess the energetic distribution across the logarithmic frequency domain. Since the integral of these curves against logarithmic frequency is proportional to the signal variance, one can extract where significant energy is present within the signal. This shows that despite the differences between the spectra in Figure 25 both spectra exhibit remarkably similar form, with a a clearly defined symmetrical peak that contains the bulk of energies. To robustly characterize the frequency of the peak a 'central frequency' (f_0) is defined for each spectra as the weighted center-of-mass of each spectral distribution (*i.e.*, the first moment) when plotted in pre-multiplied form over a logarithmic frequency domain. This frequency closely resembles the frequency of the peak owing to the symmetrical nature of the spectra. The amplitude of freestream noise is commonly defined as the standard deviation of a given pressure signal, normalized by the mean ($p'/\bar{p}$). However, since the standard deviation can be biased by limitations across the frequency domain, a common frequency band was used for this assessment and defined relative to the central frequency, namely $0.1 < f/f_c < 10$. These derived amplitudes show that R2Ch is approximately 14% quieter than LT5 with energy centered at frequencies almost five times higher (details provided in Table4). Figure 25b also shows a measure of the peak width, calculated as a standard deviation of the energy distribution across a logarithmic frequency domain.

In Figure 25c the frequency of the spectra is scaled (by cylinder length L and freestream velocity U_∞) to define a Strouhal number that characterizes the energy distribution of the freestream noise relative to that model environment. Despite increased velocities in R2Ch, the longer model results in a small increase to the R2Ch Strouhal numbers,

(a) R2Ch. (b) LT5.

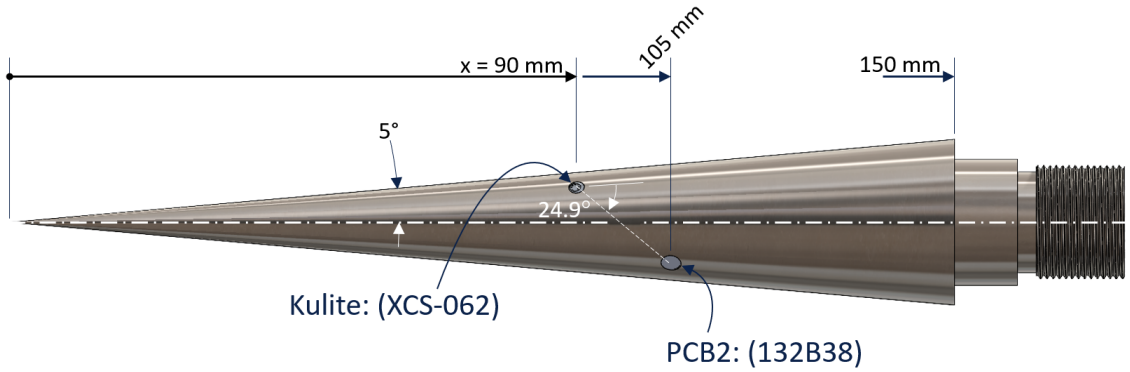

(c) Schematic diagram of 5° cone.

Fig. 24 Acoustic free-stream perturbation probe. inside R2Ch (a) and LT5 (b) and CAD of the model (c).

yielding a slightly increased difference between the two relevant environments ($\mathrm{St}_{L_{R2Ch}}/\mathrm{St}_{L_{LT5}} \approx 6.3$).

Figure 25d characterizes the relative distributions by scaling frequencies by the central frequency, and amplitudes by the band-limited variance of pressure. When overlaid, it is clear that, while similar, the shapes differ between each facility with the spectral peak observed in LT5 being slightly wider (by 11%). Distribution skewness remains small in both cases, with the maximum values for the third standardized moment (skewness normalized by variance) of -0.098 and +0.117 for R2Ch and LT5, respectively. Statistics of the spectral peaks are shown in Table 4.

It should be noted that since unit Reynolds numbers for freestream characterization differ from the comparable HCF testing conditions (−8% for LT5, +69% for R2Ch) some interpretation of the spectra is required when framing the anticipated freestream noise environment acting upon the HCF. If Re' from the freestream characterization is higher than that of the HCF experiment then one would expect larger boundary layers, and thus be characterized by lower frequencies. However, since the side-wall boundary layers presumably driving the freestream spectra are turbulent, this effect may be small, *i.e.* if $f \propto 1/\delta \propto 1/\mathrm{Re}_x^{1/7}$. By this logic, the +69% difference in the R2Ch Reynolds number would drop the frequency by 8% to approximately 22.7 kHz, in LT5 this would have less an effect, increasing frequency by 1% to 5.00 kHz.

While there are numerous studies on the amplitude scaling of wind tunnel noise [47, 48], accurate experimental data on its frequency scaling is still lacking. Numerous numerical studies, however, document a frequency scaling of the emited noise as $f \propto U_e/\delta$ [49, 50], with U_e the nozzle boundary layer edge velocity, and δ the nozzle boundary layer thickness. While one could expect small variation in U_e (which is assumed to be scaling like U_∞ for the present study) due to either a difference in facility Mach number or stagnation temperature, the main possible source of discrepancies could come from the difference in nozzle wall boundary layer thicknesses. Figure 27 presents the nozzle profile of the two facilities on a common figure, the LT5 nozzle[51] is more than two times longer than the R2Ch one, which means

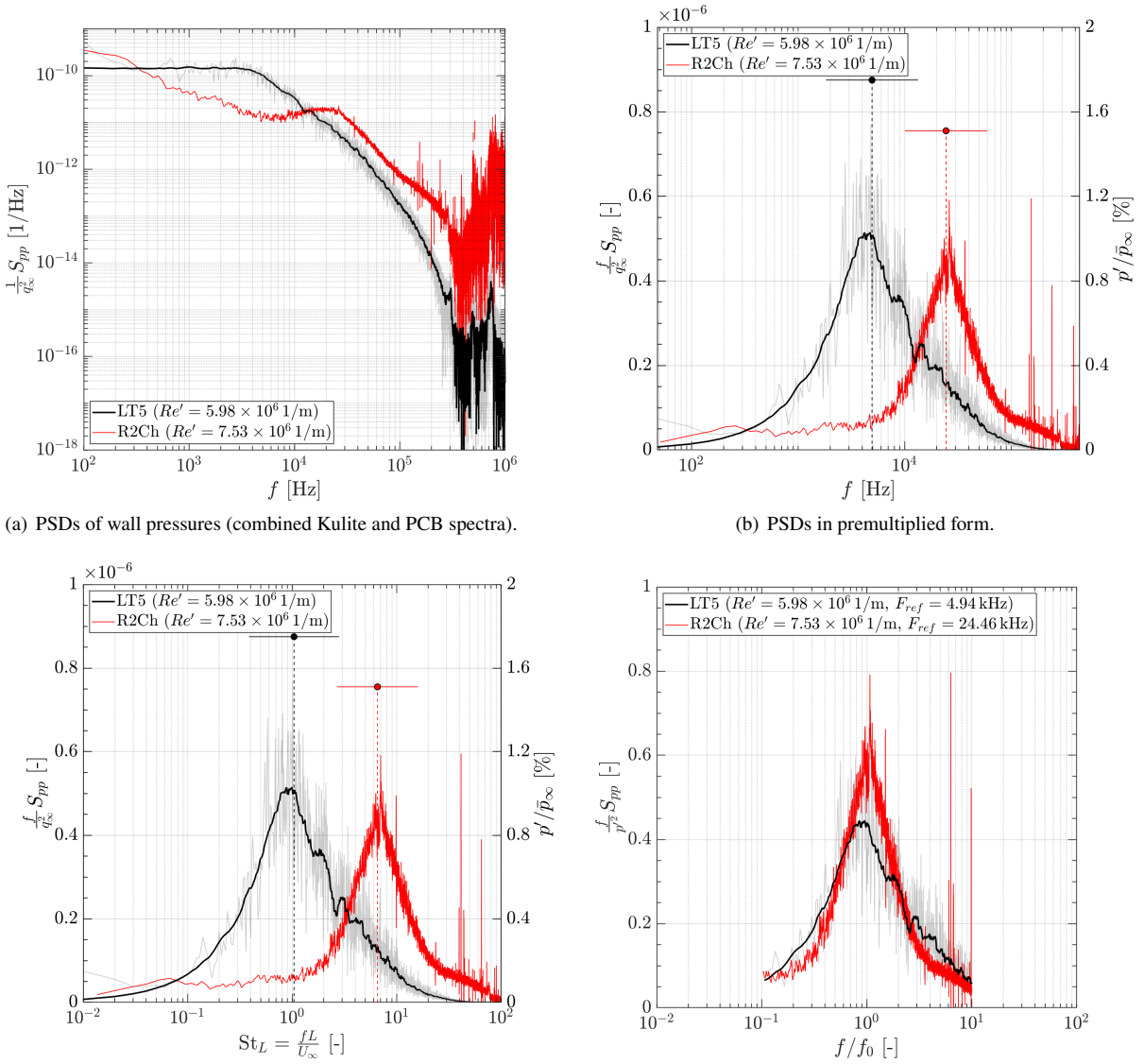

(a) PSDs of wall pressures (combined Kulite and PCB spectra).

(b) PSDs in premultiplied form.

(c) PSDs with frequency normalized to Strouhal number.

(d) PSDs normalized by central frequency (f_0) and amplitude ($p'/\bar{q}_\infty$).

Fig. 25 Comparison of freestream noise environments between R2Ch and LT5 at comparable values of $\mathrm{Re}_L \approx 1.1 \times 10^6$. Standard deviation of logarithmic frequency distribution indicated by horizontal line spanning $\pm\sigma\left(\log_{10} f\right)$, at the central frequency (f_0) and plotted against right axis showing integral unsteadiness ($p'/\bar{p}_\infty$).

that for the same unit free-stream Reynolds number, one could expect the nozzle wall boundary layer of R2Ch to be much thinner, and thus the emitted acoustic noise to be at higher frequency.

While this shift in frequency goes in the expected direction, it would be interesting to get actual quantitative data to compare the expected ratio of mean frequency of the emitted noise given the scaling parameters and the measured data. In order to do that, experimental measurements of nozzle exit boundary layer at LT5 coming from [51] are compared to data coming from RANS simulations of the R2Ch nozzle. One has to keep in mind that there are multiple sources of uncertainty in the data used to compute the frequency scaling, first for LT5, the proper evaluation of δ_{99} from experimental data is complex, then for R2Ch, the RANS computation supposes fully turbulent flow in the whole nozzle, while in reality the flow probably transitions along the nozzle profile. As such, the scaling presented hereafter should be considered only as an order of magnitude. The nozzle boundary layer thickness and the free-stream velocity are presented in table 5, the nozzles length difference lead to a boundary layer that is more than two times thinner in R2Ch.

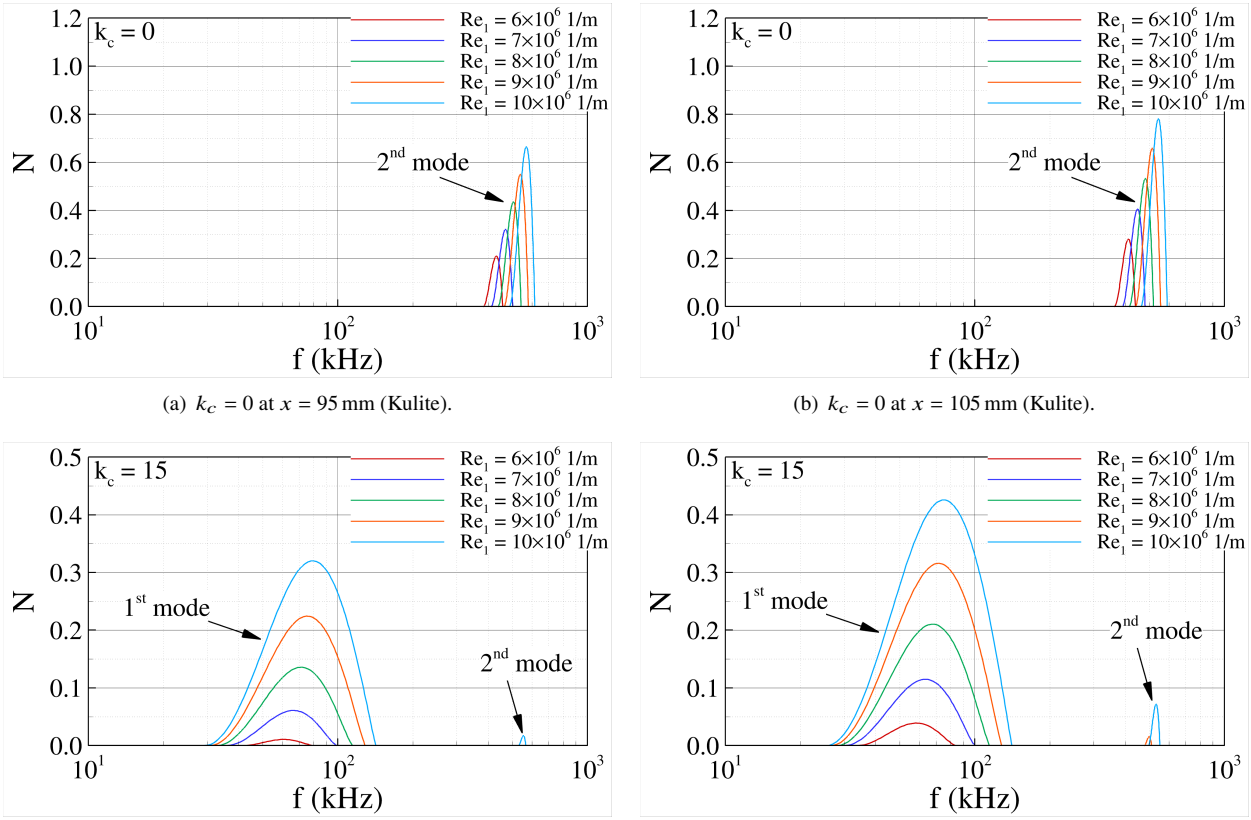

(a) $k_c = 0$ at $x = 95$ mm (Kulite).

(b) $k_c = 0$ at $x = 105$ mm (Kulite).

(c) $k_c = 15$ at $x = 95$ mm (Kulite).

(d) $k_c = 15$ at $x = 105$ mm (PCB).

Fig. 26 LST N-factors for 5° sharp cone at $M_\infty = 4.82$ across a range of Reynolds numbers.

Facility	$f_0\,(\log_{10} f)$	St_L	$p'/\bar{q}_\infty$	$p'/\bar{p}_\infty$	$\sigma\,(\log_{10} f)$	$\tilde{\mu}_3\,(\log_{10} f)$
LT5	4.94 kHz	1.04	0.108%	1.75%	0.431	+0.117
R2Ch	24.45 kHz	6.54	0.087%	1.51%	0.387	−0.098

Table 4 Characterization of freestream noise spectral statistics in each facility at comparable values of $\mathbf{Re}_L \approx 1.1 \times 10^6$.

As such, and also taking into account the differences in free-stream velocity, the noise emitted at the outlet of R2Ch should be at a frequency 2.5 times larger than at the outlet of LT5.

However, the measurements presented in Section III.A were conducted at the center of the outlet plane of the nozzle, and thus are not measurements of the noise emitted at the outlet but at an upstream position in the nozzle. To get the proper emission point, one can follow a characteristic line (see figure 27). This may strongly impact the scaling given that the boundary layer development length between the throat and emission point is almost half of the nozzle length in R2Ch, while for LT5 it should be way less impactful given that the reduction will be less important when compared with the nozzle length. As such, one can recompute the scaling by using the boundary layer thickness at the emission point (for LT5, because of the lack of data and the fact that the expected change is small, the data is unchanged), leading to an expected frequency for R2Ch more than 4.2 times larger than the one of LT5, which is close to the measured value.

Now that the difference in acoustic noise has been measured and potential origin for the discrepancies have been discussed, one can discuss the impact it may have on the transition process and thus the separated region size differences discussed in section III.A.1. Previous studies [23] have shown that one of the likely transition scenario for such flow includes the linear growth (and non-linear interaction) of first mode and shear layer instabilities. From those results, the expected frequency range of the instabilities for the Reynolds number of interest here can be estimated to be between

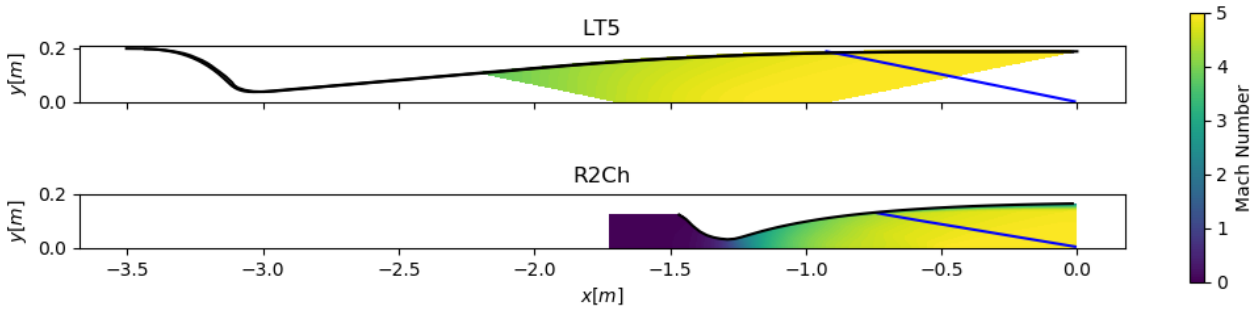

Fig. 27 Illustration of nozzle profiles for both facilities[51] The blue line corresponds to the characteristic line along which the emitted noise measured by the cone travels.

Facility	U_∞	Nozzle Exit			Emission Point		
		δ_0	f_{R2Ch}/f_{LT5}	$\mathrm{St}_{L_{R2Ch}}/\mathrm{St}_{L_{LT5}}$	δ_0	f_{R2Ch}/f_{LT5}	$\mathrm{St}_{L_{R2Ch}}/\mathrm{St}_{L_{LT5}}$
LT5	846 m/s	55 mm	2.5	3.2	55 mm	4.2	5.3
R2Ch	950 m/s	25 mm			15 mm		

Table 5 Scaling of the noise frequency in both facilities. Ratios of Strouhal number indicate estimated effect on HCF models.

10 and 60 kHz (for a slightly higher Reynolds number, [23] found a most amplified first mode wave at 51 kHz in the attached boundary layer and shear layer mode at 15 kHz in the shear layer on top of the recirculation region).

Given that those instabilities are convective mode, they are subject to receptivity and thus, the wind tunnel noise emitted in the $10-60$ kHz range should be the most impactful on their development. A high noise in that range should lead to a higher seeding of those modes, which in turn would lead to higher amplitude and could thus cause faster transition. Going back to the experimental results presented Figure 25, one can notice that the R2Ch measurements display a significantly higher energetic content in the range of interest. Because of that, even if the overall noise level of R2Ch (1.51%) is slightly lower than the one of LT5 (1.75%), the R2Ch noise should lead to a higher initial amplitude of the modes at the origin of transition and thus to a transition happening sooner in R2Ch than in LT5, which would be characterized by a noticeably smaller recirculation region. This result is coherent with the experimental observation presented in section III.A.1 and could explain the differences between the experiments run at R2Ch and at LT5. It is important to note that this represents the first documented case where using traditional noise quantification technique alone (in % of the Pitot or free-stream pressure) would lead to an erroneous conclusion because of the differences in spectral content of the noise.

IV. Conclusions

The flow over a HCF at Mach 5 with 15° flare deflection has been investigated in an internationally collaborative research effort conducted as part of the NATO STO AVT-346 Research Task Group. At the core of the investigation is the comparison of two parallel wind tunnel experiments conducted in LT5 at University of Arizona (Tucson, USA) and R2Ch at ONERA (Meudon, France). IRT was used in both tests to characterize the peak in heat transfer observed on the flare surface, associated with flow reattachment. Despite seemingly similar geometries and testing environments, a considerable scaling shift was observed when comparing the two tests, indicating that reattachment (and thus SBLI length scales in general) for the LT5 tests were almost twice as large as those for the R2Ch tests. This disparity drove the present investigation to understand why there was such a large difference, and was supported by simulations from the University of Arizona, the Technical University of Munich, and ONERA. When quantifying these differences in the remainder of this section, the experiments of R2Ch will be considered the reference, with comments on the contributing factors that would scale the LT5 experiment differently.

It has been demonstrated that mild differences in the freestream conditions will result in increased growth of the LT5 laminar boundary layer, disregarding bluntness effects (considered later). The combined effect of the reduction in

Mach number ($M_\infty = 4.82$ *v.s.* 5.0) and the increased wall temperature ($T_w/T_0 = 0.69$ *v.s.* 0.54 result in a boundary layer that is approximately 10% larger (±5% depending on the precise definition of the boundary layer thickness). The variation in Mach number also impacts the strength of the interaction, since the flare deflection angle is equal between the two cases, giving an increase pressure rise of 1.6%. Finally, each model was constructed with a different normalized cylinder diameter due to limitations of the facility. The LT5 cylinder was larger ($D/L = 1.00$ *v.s.* 0.52) resulting in a reduced 3D relief effect on the conical flare surface, marginally increasing the pressure rise further by 1.3%. Since both incoming boundary layer thickness and interaction strength have been demonstrated to scale proportionally with the SBLI length scales, these effects result in a net increased scaling of 13%.

An aspect of experimental models that was considerably different was that of the leading edge bluntness, despite initial attempts to have both geometries 'nominally sharp', with the R2Ch leading edge radius of 27 μm being considerably smaller than LT5's 102 μm. This difference is exacerbated when scaled by the model length ($r_{nose}/L = 5.7 \times 10^{-4}$ *v.s.* 1.1×10^{-4}). Simulations of this effect show a profound difference, with separation lengths increasing by approximately 37%. However, an important caveat should be discussed before final conclusions are drawn. Simulations of the R2Ch conditions were performed at Reynolds numbers of $\mathrm{Re}' = 7.5 \times 10^6\ \mathrm{m}^{-1}$ rather than $\mathrm{Re}' = 4.4 \times 10^6\ \mathrm{m}^{-1}$ in the actual experiment. This increased Re' would be expected to result in a 23% decrease in the boundary layer length scales, significantly mitigating the separation length differences otherwise indicated (assuming $L_{sep} \propto \delta$), returning a modified increased length scale of only 6%. It should also be noted that these simulations included effects of differences in wall temperature, cylinder diameter, and Mach number, meaning the effect of bluntness alone could still be over-represented. Regardless, the combined effect of all factors mentioned up until this point is an increased length scale of approximately 20%, still significantly below the 90% difference observed in the experimental results. Further work has to be conducted to clarify this matter.

In order to simulate a 'conventional' ('noisy') wind tunnel environment, simulations were carried out where a wide range of disturbance waves are forced by introducing random fluctuations at the inflow of the computational domain. Simulations carried out at ONERA and TU Munich show that the freestream noise has a significant effect on the separation and reattachment location. By tuning the 'noise' amplitude in the simulations both ONERA and TU Munich are able to match the separation and reattachment location measured in the ONERA experiments. To quantify the impact of freestream noise on the separation length in the experiments, the noise level and the spectrum 'shape' in the simulations in future sudies will be modeled according to the spectra measured in the R2Ch and LT5.

Measurements of the noise environment in each facility indicated considerable differences which may be significant when considering the impact of this simulated noise on the experimental results. Freestream noise was characterized using a 5° half-angle cone to attempt to measure static pressure fluctuations directly, as opposed to the standard Pitot probe approach. When noise is reported in the standard form of a percentage of the mean value each facility appears similar with LT5 exhibiting $p'/\bar{p}_\infty = 1.75\%$ *v.s.* R2Ch's level of 1.51% (assessed over ± one decade from the log-weighted central frequency). When considered in pre-multiplied form, it became evident that each noise distribution was remarkably similar ($\sigma(\log_{10} f) \approx 0.4$ with minimal skew in logarithmic domain), albeit shifted to much lower frequencies in LT5 ($f_0 = 4.94$ kHz for LT5 *v.s.* 24.45 kHz for R2Ch. When scaled by freestream velocity and cylinder length, this resulted in a Strouhal number reduction of $\mathrm{St}_{R2Ch}/\mathrm{St}_{LT5} = 6.3$. The cause of this discrepancy was investigated and linked to the length scale of the nozzle wall turbulent boundary layer at the point of emission before radiating to the model. Since the LT5 nozzle is considerably longer (approx. 2× of normalized length L_{nozz}/D_{nozz}), this results in a larger boundary layer, at the wall location of an upstream projected characteristic line. When combined with slight differences in freestream velocities this resulted in an estimated frequency ratio of $f_{R2Ch}/f_{LT5} = 4.2$, acting to somewhat explain the disparity in observed spectra. When considering the impact of this on the HCF flow, this ratio of frequencies can be scaled to a ratio of cylinder length Strouhal numbers where $\mathrm{St}_{L_{R2Ch}}/\mathrm{St}_{L_{LT5}} = 5.3$.

Future work is planned to finalize this investigation and conclude the effects of realistic noise environments on the HCF SBLI utilizing well-executed simulations and theory.

Acknowledgments

The University of Arizona would like to thank the US Navy's Office of Naval Research (ONR) and program manager Dr. Eric Marineau for providing funding for this work (N00014-20-1-2267). In addition, the authors would like to recognize the contribution of Ashish Singh, Sathyan Padmanabhan, Alejandro Roskelley Garcia, and Sam Bevier for their assistance when operating the test facility. The authors would also like to express their gratitude to Prof. Alex Craig for providing nozzle data from LT5.

Mathieu Lugrin would like to thank Eric Garnier, Ivan Mary, Cedric Content and Bruno Maugars for the discussions

on numerical method as well as ONERA for providing a 1M CPU hours allocation for young researchers from ONERA to run the DNS. The R2Ch team is acknowledged for the help they provided to gather the experimental data. This work was partially supported by the French Alternative Energies and Atomic Energy Commission (CEA) under the grant CEA 4600334751.

The TUM authors gratefully acknowledge the Gauss Centre for Supercomputing e.V. (www.gauss-centre.eu) for funding this project by providing computing time on the GCS Supercomputer SuperMUC-NG at Leibniz Supercomputing Centre (www.lrz.de).

References

[1] Chapman, D. R., Kuehn, D. M., and Larson, H. K., "Investigation of separated flows in supersonic and subsonic streams with emphasis on the effect of transition," Tech. rep., NACA, Moffett Field, CA, 1958. URL http://hdl.handle.net/2060/19930092343.

[2] Becker, J. V., and Korycinski, P. F., "Heat Transfer and Pressure Distribution at a Mach Number of 6.8 on Bodies with Conical Flares and Extensive Flow Separation," , 1956.

[3] Ginoux, J. J., "On Some Properties of Reattaching Laminar and Transitional High Speed Flows," *Heat and Mass Transfer in Flows with Separated Regions*, von Karman Institute, 1969.

[4] Benay, R., Chanetz, B., Mangin, B., Vandomme, L., and Perraud, J., "Shock Wave/Transitional Boundary-Layer Interactions in Hypersonic Flow," *AIAA Journal*, Vol. 44, No. 6, 2006, pp. 1243–1254. https://doi.org/10.2514/1.10512, URL http://arc.aiaa.org/doi/10.2514/1.10512.

[5] Bur, R., and Chanetz, B., "Experimental Study on the PRE-X Vehicle Focusing on the Transitional Shock-Wave/Boundary-Layer Interactions," *Aerospace Science and Technology*, Vol. 13, No. 7, 2009, pp. 393–401. https://doi.org/10.1016/j.ast.2009.09.002.

[6] Leinemann, M., Radespiel, R., Muñoz, F., Esquieu, S., McKiernan, G., and Schneider, S. P., "Boundary Layer Transition on a Generic Model of Control Flaps in Hypersonic Flow," *AIAA Scitech 2019 Forum*, AIAA, San Diego, CA, 2019, pp. 1–21. https://doi.org/10.2514/6.2019-1908, URL https://arc.aiaa.org/doi/10.2514/6.2019-1908.

[7] Cobourn, J. W., and Schmisseur, J. D., "Focused Laser Differential Interferometry Combined with Schlieren on Hypersonic Hollow Cylinder Flare and Hollow Cylinder Configurations," *AIAA Scitech 2021 Forum*, American Institute of Aeronautics and Astronautics, VIRTUAL EVENT, 2021. https://doi.org/10.2514/6.2021-0369.

[8] Lugrin, M., Nicolas, F., Severac, N., Tobeli, J. P., Beneddine, S., Garnier, E., Esquieu, S., and Bur, R., "Transitional shockwave/boundary layer interaction experiments in the R2Ch blowdown wind tunnel," *Experiments in Fluids*, Vol. 63, No. 2, 2022. https://doi.org/10.1007/s00348-022-03395-9, URL https://doi.org/10.1007/s00348-022-03395-9.

[9] Threadgill, J. A. S., Jouannais, L., Hader, C., Flood, J. T., Craig, S. A., Fasel, H. F., and Little, J. C., "Fin-induced Shock Boundary Layer Interactions on a Flat Plate and Hollow Cylinder at Mach 5," *AIAA SCITECH 2022 Forum*, American Institute of Aeronautics and Astronautics, Reston, Virginia, 2022. https://doi.org/10.2514/6.2022-1816, URL https://arc.aiaa.org/doi/10.2514/6.2022-1816.

[10] Threadgill, J. A. S., Singh, A., Roskelley Garcia, A., and Little, J. C., "Boundary Layer Separation on a Hollow-Cylinder/Flare at Mach 5," *AIAA Scitech 2023 Forum*, American Institute of Aeronautics and Astronautics, Reston, Virginia, 2023. https://doi.org/10.2514/6.2023-1246, URL https://arc.aiaa.org/doi/10.2514/6.2023-1246.

[11] SCHAEFER, J. W., and FERGUSON, H., "Investigation of Separation and Associated Heat Transfer and Pressure Distribution on Cone-Cylinder-Flare Configurations at Mach Five," *ARS Journal*, Vol. 32, No. 5, 1962, pp. 762–770. https://doi.org/10.2514/8.6146.

[12] ZAKKAY, V., and CALLAHAN, C. J., "Laminar, Transitional and Turbulent Heat Transfer to a Cone-Cylinder-Flare Body at Mach 8.0," *Journal of the Aerospace Sciences*, Vol. 29, No. 12, 1962, pp. 1403–1413. https://doi.org/10.2514/8.9857.

[13] Benitez, E. K., Jewell, J. S., and Schneider, S. P., "Separation Bubble Variation Due to Small Angles of Attack for an Axisymmetric Model at Mach 6," *AIAA Scitech 2021 Forum*, 2021. https://doi.org/10.2514/6.2021-0245.

[14] Wagner, L. N., Schneider, S. P., and Jewell, J. S., "Streamwise Vortices from Controlled Roughnesses on a Cone-Cylinder-Flare at Mach 6," *AIAA Scitech 2022 Forum*, American Institute of Aeronautics and Astronautics, San Diego, CA & Virtual, 2022. https://doi.org/10.2514/6.2022-1671.

[15] Holden, M., "Shock Interaction Phenomena in Hypersonic Flows," *29th AIAA, Plasmadynamics and Lasers Conference*, American Institute of Aeronautics and Astronautics, Albuquerque, NM, U.S.A., 1998. https://doi.org/10.2514/6.1998-2751.

[16] Dieudonne, W., Boerrigter, H., and Charbonnier, J., "Hypersonic flow on a blunted cone-flare model and in the VKI-H3 Mach 6 wind tunnel," *von Karman Institute Technical Note 193*, 1997.

[17] Running, C. L., Juliano, T. J., Borg, M. P., and Kimmel, R. L., "Characterization of Post-shock Thermal Striations on a Cone/Flare," *AIAA Journal*, Vol. 58, No. 5, 2020, pp. 2352–2358. https://doi.org/10.2514/1.J059095.

[18] Butler, C. S., and Laurence, S. J., "Transitional Hypersonic Flow over Slender Cone/Flare Geometries," *Journal of Fluid Mechanics*, Vol. 949, 2022, pp. 1–45. https://doi.org/10.1017/jfm.2022.769.

[19] Cao, S., Hao, J., Klioutchnikov, I., Olivier, H., and Wen, C.-Y., "Unsteady effects in a hypersonic compression ramp flow with laminar separation," *Journal of Fluid Mechanics*, Vol. 912, 2021, p. A3.

[20] Lugrin, M., Beneddine, S., Garnier, E., and Bur, R., "Multi-scale study of the transitional shock-wave boundary layer interaction in hypersonic flow," *Theoretical and Computational Fluid Dynamics*, Vol. 36, 2022, pp. 277–302.

[21] Hao, J., Cao, S., Wen, C.-Y., and Olivier, H., "Occurrence of global instability in hypersonic compression corner flow," *Journal of Fluid Mechanics*, Vol. 919, 2021, p. A4.

[22] Cao, S., Hao, J., Klioutchnikov, I., Olivier, H., Heufer, K. A., and Wen, C.-Y., "Leading-edge bluntness effects on hypersonic three-dimensional flows over a compression ramp," *Journal of Fluid Mechanics*, Vol. 923, 2021, p. A27.

[23] Lugrin, M., Beneddine, S., Leclercq, C., Garnier, E., and Bur, R., "Transition scenario in hypersonic axisymmetrical compression ramp flow," *Journal of Fluid Mechanics*, Vol. 907, 2021, p. A6.

[24] Dwivedi, A., Sidharth, G., Nichols, J. W., Candler, G. V., and Jovanović, M. R., "Reattachment streaks in hypersonic compression ramp flow: an input–output analysis," *Journal of Fluid Mechanics*, Vol. 880, 2019, pp. 113–135.

[25] Hao, J., Cao, S., Guo, P., and Wen, C.-Y., "Response of hypersonic compression corner flow to upstream disturbances," *Journal of Fluid Mechanics*, Vol. 964, 2023, p. A25.

[26] Flood, J. T., Hader, C., Skora, A., Fasel, H. F., and Craig, S. A., "Experimental measurements and numerical investigations of boundary-layer instabilities on a Mach 4.82 hollow cylinder," *AIAA SciTech 2023 Forum*, 2023.

[27] Le Sant, Y., Marchand, M., Millan, P., and Fontaine, J., "An overview of infrared thermography techniques used in large wind tunnels," *Aerospace Science and Technology*, Vol. 6, No. 5, 2002, pp. 355–366. https://doi.org/10.1016/S1270-9638(02)01172-0.

[28] Laible, A. C., Mayer, C. S. J., and Fasel, H. F., "Numerical investigation of supersonic transition for a circular cone at Mach 3.5," *38th Fluid Dynamics Conference and Exhibit*, 2008. AIAA 2008-4397.

[29] Mayer, C., Von Terzi, D. A., and Fasel, H. F., "Direct numerical simulation of complete transition to turbulence via oblique breakdown at Mach 3," *Journal of Fluid Mechanics*, Vol. 674, 2011, pp. 5–42.

[30] Sivasubramanian, J., and Fasel, H. F., "Direct numerical simulation of transition in a sharp cone boundary layer at Mach 6: fundamental breakdown," *Journal of Fluid Mechanics*, Vol. 768, 2015, pp. 175–218.

[31] Hader, C., and Fasel, H. F., "Direct Numerical Simulations of Hypersonic Boundary-Layer Transition for a Flared Cone: Fundamental Breakdown," *Journal of Fluid Mechanics*, Vol. 869, 2019.

[32] Chakravarthy, S., Peroomian, O., Goldberg, U., and Palaniswamy, S., "The CFD++ computational fluid dynamics software suite," *AIAA and SAE, 1998 World Aviation Conference*, 1998, p. 5564.

[33] Hader, C., and Fasel, H. F., "Towards simulating natural transition in hypersonic boundary layers via random inflow disturbances," *Journal of Fluid Mechanics*, Vol. 847, 2018. https://doi.org/10.1017/jfm.2018.386.

[34] Mary, I., and Sagaut, P., "Large Eddy Simulation of Flow Around an Airfoil Near Stall," *AIAA Journal*, Vol. 40, No. 6, 2002, pp. 1139–1145. https://doi.org/10.2514/2.1763, URL https://doi.org/10.2514/2.1763.

[35] Vos, J., Duquesne, N., and Lee, H., "Shock wave boundary layer interaction studies using the NSMB flow solver," 3rd European Symposium on Aerothermodynamics for Space Vehicles, ESA SP-426, 1999.

[36] Stemmer, C., Birrer, M., and Adams, N., "Hypersonic Boundary-Layer Flow with an Obstacle in Thermochemical Equilibrium and Nonequilibrium," *Journal of Spacecraft and Rockets*, Vol. 54(4), 2017, pp. 899–915. URL https://doi.org/10.2514/1.A32984.

[37] Di Giovanni, A., and Stemmer, C., "Cross-flow-type breakdown induced by distributed roughness in the boundary layer of a hypersonic capsule configuration," *Journal of Fluid Mechanics*, Vol. 856, 2018, pp. 470–503. URL https://doi.org/10.1017/jfm.2018.706.

[38] Chiapparino, G., and Stemmer, C., "Numerical investigation of a Mach 6 laminar shock-wave/boundary-layer interaction on a two-dimensional ramp with 3D controlled surface roughness," *International Journal of Heat and Fluid Flow*, Vol. 103, 2023, p. 109193. URL https://doi.org/10.1016/j.ijheatfluidflow.2023.109193.

[39] Souverein, L. J., Bakker, P. G., and Dupont, P., "A scaling analysis for turbulent shock-wave/boundary-layer interactions," *Journal of Fluid Mechanics*, Vol. 714, 2013, pp. 505–535. https://doi.org/10.1017/jfm.2012.495, URL http://www.journals.cambridge.org/abstract{_}S0022112012004958.

[40] Morgan, B. E., Duraisamy, K., Nguyen, N., Kawai, S., and Lele, S. K., "Flow physics and RANS modelling of oblique shock/turbulent boundary layer interaction," *Journal of Fluid Mechanics*, Vol. 729, No. 2013, 2013, pp. 231–284. https://doi.org/10.1017/jfm.2013.301.

[41] Bertin, J. J., *Hypersonic aerothermodynamics*, AIAA, 1994.

[42] Chynoweth, B., "A new roughness array for controlling the nonlinear breakdown of second-mode waves at Mach 6," Ph.D. thesis, Purdue University, 2015.

[43] Jaunet, V., Debiève, J.-F., and Dupont, P., "Length Scales and Time Scales of a Heated Shock-Wave/Boundary-Layer Interaction," *AIAA Journal*, Vol. 52, No. 11, 2014, pp. 2524–2532. https://doi.org/10.2514/1.J052869.

[44] Haas, A., Hader, C., and Fasel, H., "Effects of Small Leading-Edge Bluntness on High-Speed Boundary-Layer Instabilities on Flat Plates," *AIAA Journal*, 2023, pp. 1–13.

[45] Chuvakhov, P., Borovoy, V. Y., Egorov, I., Radchenko, V., Olivier, H., and Roghelia, A., "Effect of small bluntness on formation of Görtler vortices in a supersonic compression corner flow," *Journal of Applied Mechanics and Technical Physics*, Vol. 58, 2017, pp. 975–989.

[46] Mack, L. M., "Boundary-layer linear stability theory," *AGARD rep*, Vol. 709, No. 3, 1984, pp. 1–3.

[47] Laufer, J., "Aerodynamic Noise in Supersonic Wind Tunnels," *Journal of Aerospace Sciences*, Vol. 28, No. 9, 1961, pp. 685–692. https://doi.org/10.2514/8.9150.

[48] Laufer, J., "Some Statistical Properties of the Pressure Field Radiated by a Turbulent Boundary Layer," *Physics of Fluids*, Vol. 7, No. 8, 1964, pp. 1191–1197. https://doi.org/10.1063/1.1711360.

[49] Hildebrand, N., Choudhari, M. M., Deegan, C. P., Huang, J., and Duan, L., "Direct numerical simulation of acoustic disturbances in a hypersonic two-dimensional nozzle configuration," *AIAA Journal*, Vol. 60, No. 6, 2022, pp. 3452–3463.

[50] Hildebrand, N., Choudhari, M. M., and Duan, L., "Reynolds-Number Effects on the Acoustic Disturbance Environment in a Mach 6 Nozzle," *AIAA Journal*, Vol. 61, No. 11, 2023, pp. 4783–4796.

[51] Bearden, K. P., Padilla, V. E., Taubert, L., and Craig, S. A., "Calibration and performance characterization of a Mach 5 Ludwieg tube," *Review of Scientific Instruments*, Vol. 93, No. 8, 2022.